8-2016

The Defects Chemsitry in La Filled CoSb3 Skutterudites Explored by Thermoelectric Study and Density Functional Theory Calculations

Xiaoyu Zeng
Clemson University

Recommended Citation

Zeng, Xiaoyu, "The Defects Chemsitry in La Filled CoSb3 Skutterudites Explored by Thermoelectric Study and Density Functional Theory Calculations" (2016). *All Dissertations*. 1683.
https://tigerprints.clemson.edu/all_dissertations/1683

THE DEFECTS CHEMISTRY IN La FILLED $CoSb_3$ SKUTTERUDITES EXPLORED BY THERMOELECTRIC STUDY AND DENSITY FUNCTIONAL THEORY CALCULATIONS

A Dissertation
Presented to
the Graduate School of
Clemson University

In Partial Fulfillment
of the Requirements for the Degree
Doctor of Philosophy
Physics

by
Xiaoyu Zeng
August 2016

Accepted by:
Dr. Terry M. Tritt, Committee Chair
Dr. Jian He
Dr. Donald Liebenberg
Dr. Catalina Marinescu

Abstract

With the ever increasing consumption rate of energy, we will run out of fossil fuel resources sooner than we expect. Also the environmental concerns associated with the use of fossil fuel become a severe issue. As such, the need for alternative energy becomes extremely impending. Thermoelectricity is the simplest technology applicable to direct heat-electricity energy conversion with electricity being the best quality form of energy and heat being the lowest. However, comparing to the front row candidates such as wind, photovoltaics, solar heat and biofuel that is possible to replace fossil fuel, thermoelectrics has received less heed due to its low conversion efficiency. Nonetheless, its ability to directly convert heat into electricity in an all solid-state manner still makes it pretty tempting for application as one of the energy sources. This can be well-justified by the fact that a huge amount of heat exhausted from a car, a power station or an industrial process is all amendable to thermoelectric (TE) conversion. What's more, TE energy conversion is green and environmentally friendly, the TE devices have no movable parts and are susceptible to be miniaturized, so they can be shaped as needed and maintenance is minimized.

Since modern TE study is efficiency driven and material oriented fundamental research, developing higher performance TE materials has thus become the ultimate goal so as to make thermoelectricity a crucial part in this big energy picture.

Among the state of art TE materials, Co_4Sb_{12} based skutterudites have become in-

creasingly favorable for room temperature (300 K) to 800 K applications. The interest mainly lies on how such high performance is achieved via "engineering" its unique crystal structure - the naturally formed nano-sized "cage". Properties of Co_4Sb_{12} based skutterudites can be "tuned" by filling guest atoms and/or substitutionally doping. The function of guest atoms is two-fold: One is to decrease the lattice thermal conductivity; the other is to improve the electrical properties. While guest atoms directly help optimize TE properties, they have certain solubility limit or Filling fraction limit (FFL) in the "cage", if surpassed, secondary phases would still contribute constructively to TE performance. From a solid state physics point of view, those fillers, dopants and secondary phases are all defects of different dimensionality, therefore, Co_4Sb_{12} skutterudites provide a material template to study the interplay of defects.

Recently, the study of "cagey" material mainly focuses on the optimization of performance of "multiple-filled" skutterudites. In contrast, single filling is less sufficiently studied. To study the defect chemistry, a combined theoretical and experimental study of the single filled skutterudites is indispensable. Also, although the single-filled Co_4Sb_{12} may not exhibit high performance, understanding a high performance material is equally important as understanding a low performance material. To this end, La was chosen to be the guest atom in our work for being the first element in rare earth group and not having *f* electrons, which make theoretical calculations more feasible. So the work herein presented:

1) Experimentally using only one control variable La to implement the filling-doping-nanocomposite approach that can significantly enhance the TE efficiency compared to an unfilled one.

2) Theoretically studying the interplay between defects, i.e., the filler atoms and sb vacancies, that cannot be unequivocally interpreted by experiments.

More specifically, despite the elements normally filled into the "cage" are rare earth elements (Ce,Pr,Nd and Eu) and are named "rattler" - by definition, they are weakly bounded in the cages and "rattle" about their equilibrium position substantially more than the other atoms in the structure - but the study on "rattlers" always focus on their influence on thermal properties yet scarcely on electrical properties. Therefore, this dissertation seeks to answer questions about:

i) the physical identity of the filler, whether it is a real filler or a "rattler".
ii) The influence of f electrons on the rattling behavior.
iii) how does the interplay between the filler atoms and Sb deficiency affect the TE properties in the system.

We combine a series of experiment study with Density Functional Theory (DFT) calculations. The result not only show a obvious enhancement of TE efficiency compared to the prisine Co_4Sb_{12} skutterudite, but also revealing an approach to help further improve the TE properties of other skutterudites and cagey materials.

Dedication

To my parents, Xia Wang and Guozhen Zeng

My best friend and soul mate Patrick Roeder

I could not have made it without their love and great encouragement

Acknowledgments

I would like to express my deep and sincere gratitude to my advisor Prof. Terry M. Tritt who trusted me when I went off trail, encouraged me when I needed it, and mentored me when I got lost. Because of him, I had the courage to continue my PhD degree, and regained faith in myself. He is the mentor for life! I also want to express my many thanks to Prof. Jian He for thousands of thoughtful and enlightening conversations, for the help with my project and for the great patience with my thesis. I would like to thank my two closest friends, Menghan Zhou and Yufei Liu, thanks for always being there for me when I needed it, thanks for the discussions about passion and life, thanks for their friendship and wish them a happy married life. To my best friend and soul mate - Patrick Roeder, thank you for the encouragement and support, love and companionship. I would also like to express my appreciation to my committee members - Dr. Jian He, Dr. Donald Liebenberg and Dr. Catalina Marinescu for their precious time. Finally, I would like to thank my parents, Xia Wang and Guozhen Zeng. Without their love, support and sacrifice, I would have not made this far!

Table of Contents

List of Tables

List of Figures

Chapter 1

Introduction

1.1 Thermoelectric effects

A discussion of thermoelectric effects naturally starts with the most fundamental thermoelectric phenomenon,i.e.,the Seebeck effect [1]. As early as 1821 [2], physicist Thomas Johann Seebeck discovered that when a loop formed by antimony (Sb) and copper (Cu) joined in two places with a temperature difference in between, current would flow in the loop (Fig 1.1). This phenomenon is named in honor of him, namely, the "Seebeck effect". More generally, if the temperature at two junctions were to kept at T_1 and T_2 (T_1>T_2) with any two dissimilar materials A and B, a voltage V will be developed, this voltage is called thermal electromotive force (emf). The magnitude of V is proportional to the temperature difference at two junctions. And the ratio of the voltage developed to the temperature gradient is related to an intrinsic property called the Seebeck coefficient (α).

$$\alpha_{ab} = \frac{dV}{dT} \tag{1.1}$$

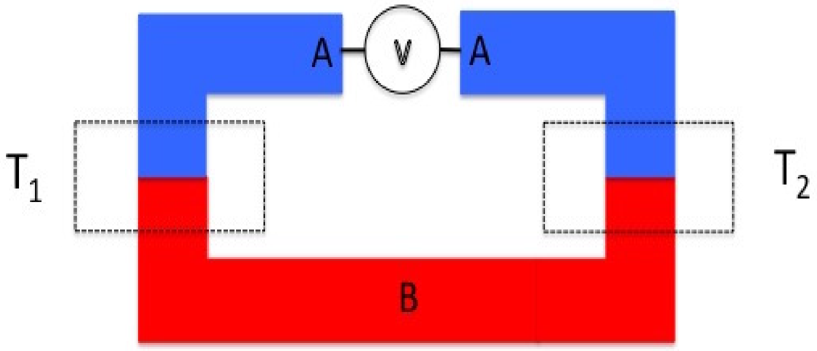

Figure 1.1: Seebeck effect: Electric potential in response to the temperature gradient ($T_1 > T_2$) applied on junctions of two dissimilar materials A and B.

where α_{ab} is the Seebeck coefficient, $dT = T_1 - T_2$. It is worth mentioning that α_{ab} can also be defined in an open-circuit circumstance.

In 1834, French physicist Jean Charles Athanase Peltier discovered that current flow through the junctions of two dissimilar conductors would cause heat absorption/release. This phenomenon is called Peltier effect [2]. It can convert electricity directly into temperature difference as is shown in Fig. 1.2 [3]. The difference of Fig. 1.2 for Peltier effect compared to Fig. 1.1 for Seebeck effect is having an external voltage yet with zero temperature gradient ($\Delta T = 0$). The heat dQ it produces in time interval dt is proportional to the current, and the ratio π_{ab} is called the Peltier coefficient:

$$dQ \propto Idt = \pi_{ab} Idt = \pi_{ab} q \tag{1.2}$$

where q is the charge transferred.

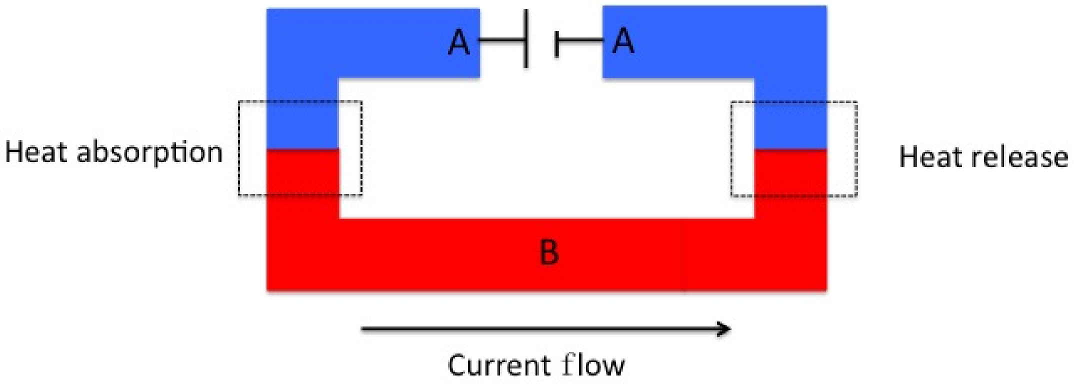

Figure 1.2: Peltier effect: cooling or heating on junctions due to a current flow without temperature difference.

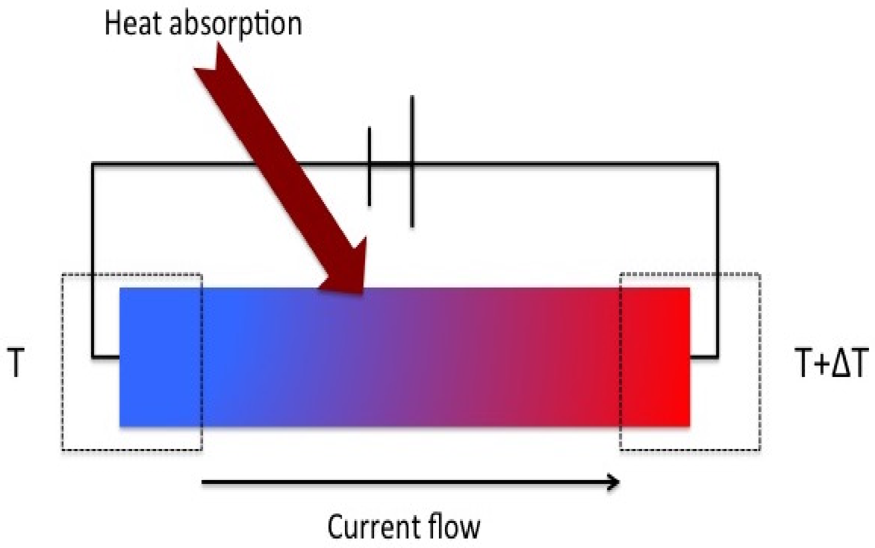

Figure 1.3: A schematic illustration of Thomson effect.

The Peltier effect has enabled the second application of thermoelectric devices - solid state refrigeration. Seebeck and Peltier effects share a subtle and fundamental connection through Thomson relation $\pi_{ab} = T\alpha_{ab}$.

The last thermoelectric effect, namely, Thomson effect [2] concerns with the heat-electricity conversion in one compositionally and thermally uniform conductor. It describes the heating or cooling of a current-carrying conductor with a temperature gradient. In 1851, Thomson discovered that when current flow through a conductor with temperature gradient, beside the Joule heat, the conductor would also absorb or release heat, this phenomenon is called Thomson effect (Fig. 1.3 [3]). The heat being absorbed or released per unit time dt is proportional to the current density J and temperature gradient ΔT:

$$\frac{dQ}{dt} = \beta J \Delta T \tag{1.3}$$

where β is called Thomson coefficient.

The above three Thermoelectric effects find a lot of applications in our daily life, especially for the Seebeck and Peltier effects, they lay the foundation of thermoelectric applications. In terms of the device configuration, it is less practical to only include one leg of the material [4], Fig. 1.4 (a) and Fig. 1.4 (b) are the TE device configuration of power generation and refrigeration respectively. Both configurations are composed of *n*-*p* leg pairs. The reason for configuring device this way is for connecting them thermally in parallel but electrically in series, so both electrons and holes are moving in the same direction pulling heat from one end to the other. In practice, many of these couples are put together (like in Fig. 1.5 [5]) for "impedance matching" in order to optimize the output power [4]. The readers are referred to appendix D for a brief review of the thermoelectric generators in history.

1.2 Performance of thermoelectric materials: figure of merit

1.2.1 Thermoelectric efficiency and gauge of performance

Thermoelectric (TE) effect lays the foundation of TE devices while the efficiency governs the applicability of devices. The efficiency of thermoelectric conversion can be defined as the ratio of output power per unit time and the received heat per unit time [2]

$$\eta = \frac{P}{Q_h} \tag{1.4}$$

The Q_h from the equation is the heat received from the hot end, P is the output power from TE device. The the current flow through the TE generator is I, the

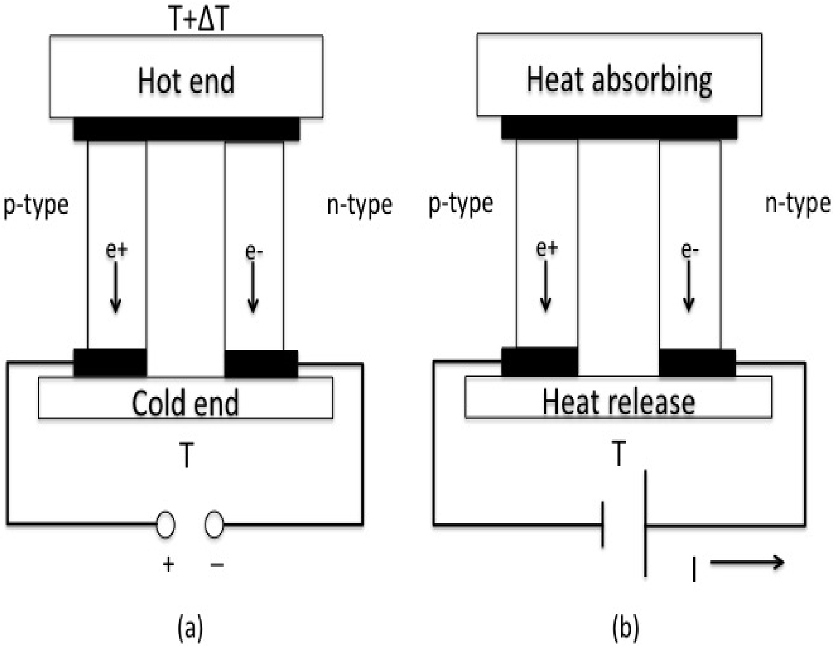

Figure 1.4: Model of thermoelectric generator and thermoelectric refrigerator [5].

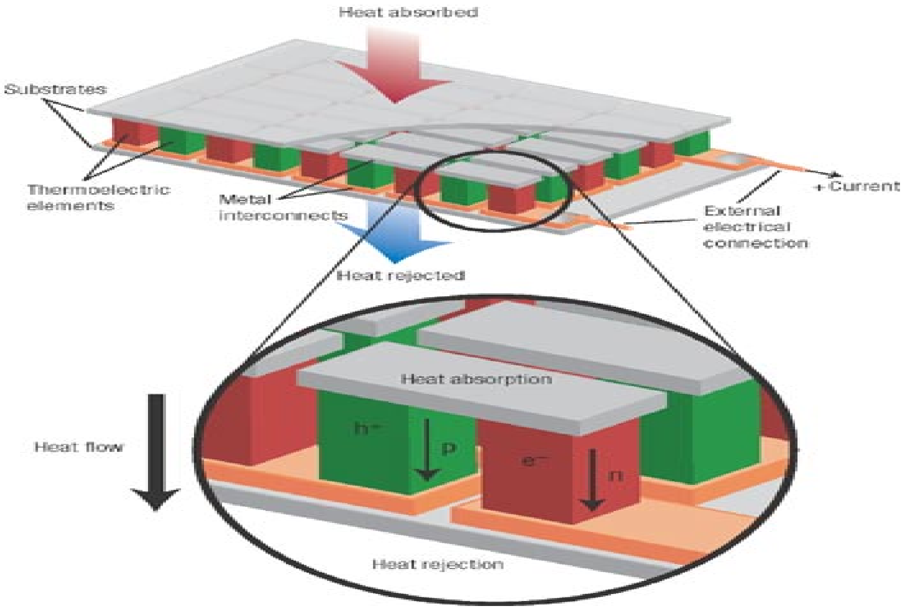

Figure 1.5: Thermoelectric module for power generation [5].

corresponding output power is:

$$P = I^2 R_L \tag{1.5}$$

where R_L is the load. Therefore, for TE generator, it should satisfy the following equation:

$$Q_h = (\alpha_p - \alpha_n) T_H I + \kappa (T_H - T_C) - \frac{I^2 R}{2} \tag{1.6}$$

So the total heat generated on the hot end is consist of heat from TE effect and heat transported away due to the heat conducting, minus the loss due to Joule heating. In the equation, T_H and T_C is the temperature from hot end and cold end respectively, and κ is the total thermal conductivity of the two legs.

$$\kappa = \frac{\lambda_P A_P}{L_P} + \frac{\lambda_n A_n}{L_n} \tag{1.7}$$

And the total Resistance R from n type part and p type part is:

$$R = \frac{L_n \rho_n}{A_n} + \frac{L_P \rho_P}{A_P} \tag{1.8}$$

Where A,L and ρ is the cross section area, length and electrical resistivity of one thermocouple leg respectively. Therefore, for the whole device, the current I can be expressed as:

$$I = \frac{(\alpha_P - \alpha_n)(T_H - T_C)}{R_L + R} \tag{1.9}$$

The corresponding efficiency can be presented as:

$$\eta = \frac{I^2 R_L}{(\alpha_P - \alpha_n)T_1 I - I^2 R/2 + \kappa(T_H - T_C)} \tag{1.10}$$

Put $M = R_L/R$,given a material, its efficiency will change with M. If taking derivative of equation 1.10 with respect to M, and put $d\eta/dM = 0$, then the highest conversion efficiency can be:

$$\eta_{max} = \frac{T_H - T_C}{T_H} \times \frac{M - 1}{M + T_C/T_H} \tag{1.11}$$

Similarly, for TE cooling, the highest coefficient of performance can be written as:

$$\phi_{max} = \frac{T_C}{T_H - T_C} \times \frac{M - T_H/T_C}{M + 1} \tag{1.12}$$

And the M in the equation is equal to $[1 + Z(T_H + T_C)/2]^{1/2}$. In which $Z = \frac{\alpha^2 \sigma}{\kappa}$. For convenience, one use ZT more often because it is dimensionless. Therefore, we herein introduced a very important intrinsic parameter that is only related to material properties, figure of merit:

$$ZT = \frac{\alpha^2 \sigma T}{\kappa} \tag{1.13}$$

where α is Seebeck coefficient, σ the electrical conductivity, κ the thermal conductivity, T the absolute temperature, and $\alpha^2\sigma$ is usually called power factor. And it is clear that ZT is the **gauge** of the material performance.

1.2.2 Thermoelectric Figure of Merit, ZT

Per the derivation above, a materials' figure of merit, or ZT is directly related to the efficiency and coefficient of performance of the material by the relation [6]

$$\eta_{max} \;\; and \;\; \phi_{max} \propto (1 + ZT)^{\frac{1}{2}} \tag{1.14}$$

Therefore, when ZT approaches infinity, η_{max} and ϕ_{max} approach the limit of the Carnot efficiency η_c. The Carnot efficiency comes from the first term of Eq. 1.11 and 1.12 ($\frac{T_H - T_C}{T_H}$ and $\frac{T_C}{T_H - T_C}$). However, modern TE devices can only achieve a small fraction of the Carnot efficiency, which makes them insufficient for applications. For example, if we assume a heat engine operating between the temperature of $T_H = 800K$ and $T_C = 300K$, Fig. 1.6 [7] shows the ratio of power generation efficiency η and Carnot efficiency η_c plotted as a function of ZT with a Carnot efficiency of 62%. This plot is used only to ascertain where the greatest return in efficiency gain would be achieved per unit increase in ZT. As we can see, the goal for an ideal ZT ranges from 2 $\sim$ 3 for the biggest return [7], since above ZT=3, the increment of η/η_C per unit ZT would get marginal. As of now, a $ZT \approx$ 2-3 is still not reachable for most TE materials. Consequently, improving ZT becomes a priority for all thermoelectric

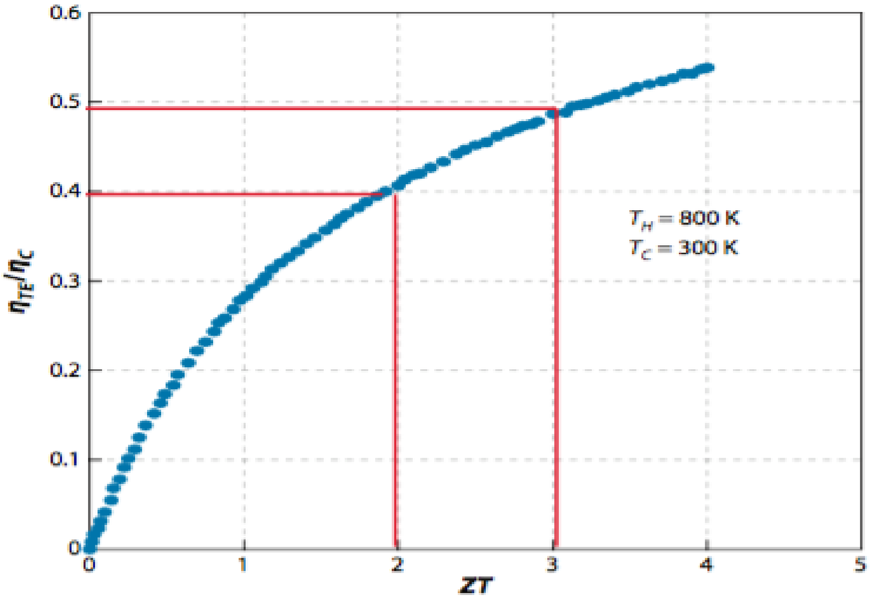

Figure 1.6: The ratio of TE efficiency to the Carnot efficiency (η/η_C) as a function of the figure of merit, ZT. The maximum efficiency or Carnot efficiency is given by $\eta_C = (T_H - T_C)/T_H = (800K - 300K)/800K = 63\%$ [7].

study. By the definition of figure of merit, $ZT = \frac{\alpha^2\sigma T}{\kappa}$, this problem is naturally shifted to optimizing three ZT-governing TE properties $\{\sigma, \alpha, \kappa\}$ in their totality.

1.3 Electrical transport in thermoelectric materials

A deep understanding of electron transport behavior including Seebeck coefficient (α) and electrical conductivity (σ) requires a deep understanding of electron band structure, Fermi Dirac statistics and Boltzmann transportation function *etc*, please refer to appendix A and B for more details about band structure and transport properties.

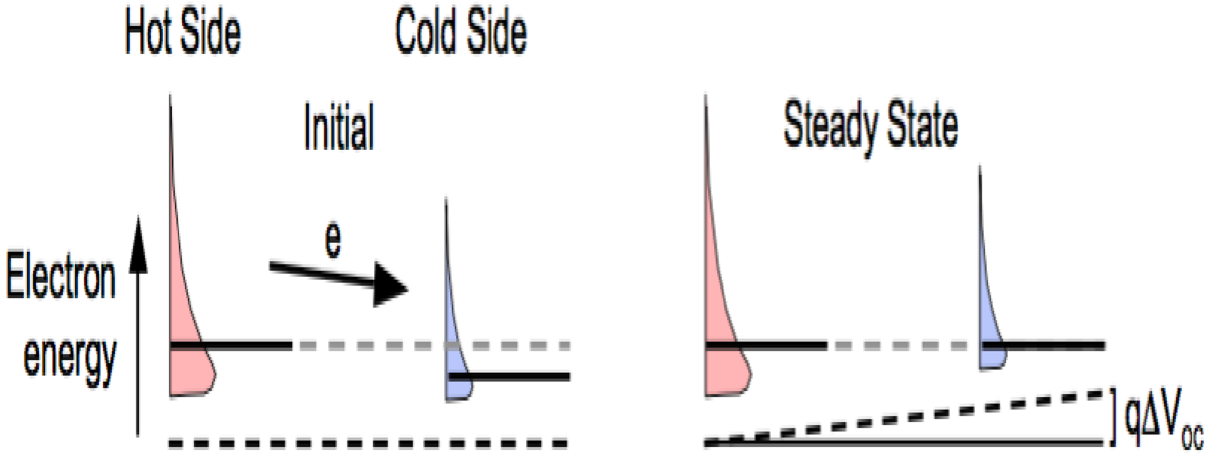

Figure 1.7: The physical explanation of Seebeck effect. [4].

1.3.1 Seebeck coefficient α and electrical conductivity σ

A macroscopic picture of α has been introduced in section 1.1, which provided a over simplified particle - wise description of how emf is a result of charge carriers flow under temperature difference. Re-visiting α using a "band structure" interpretation would bring more physical insight. Fig. 1.7 illustrates the redistribution of electrons between the hot side (red area: from the product of DOS and Fermi-Dirac distribution function) and cold side (blue area) when applying a temperature difference. Electrons with higher energy on hot side tend to "re-distribute" on the cold side resulting an opposing voltage to prevent further current flow in an open circuit circumstance. And the resulted emf is what defines the α.

In this picture, α **is the "average" entropy transported by the charge carriers**. This is consistent with the result of α derived from Boltzmann equation under quasi-equilibrium assumption:

$$\alpha = \frac{k_B}{q}\frac{\int \sigma(E)\frac{(E-E_F)}{k_BT}(-\frac{\partial f_{eq}}{\partial E})dE}{\int \sigma(E)(-\frac{\partial f_{eq}}{\partial E})dE} \propto \langle E - E_F \rangle \tag{1.15}$$

in which $-\frac{\partial f_{eq}}{\partial E}$ is Fermi "window" factor, and $\sigma(E)$ is the differential conductivity that acts as a measure of the contribution of electrons with energy E to the total conductivity. This equation implies that α is directly proportional to $\langle E - E_F \rangle$ that is exactly the "average" energy of charge carriers near Fermi level. It also implies that for a maximum α, the differential conductivity $\sigma(E)$ should be as asymmetric as possible with respect to the Fermi level, so the electrons with energies higher than Fermi Level would not cancel with the electrons with energies lower than Fermi level that lead to a zero $\langle E - E_F \rangle$ term.

The Seebeck coefficient depends on not only the band structure, i.e., the initial and final state of charge carrier to calculate the average energy, but also the intermediate scattering mechanisms between the initial and final state. The mott equation of α divided the contributions to α into two parts:

$$\alpha = \frac{\pi^2}{3}\frac{k_B^2 T}{q}[\frac{1}{n(E)}\frac{dn(E)}{dE} + \frac{1}{\mu(E)}\frac{d\mu(E)}{dE}] = \frac{\pi^2}{3}\frac{k_B^2 T}{q}[\frac{g(E)}{n(E)} + \frac{1}{\mu(E)}\frac{d\mu(E)}{dE}] \tag{1.16}$$

This equation usually applies for degenerate semiconductor in a single-band case [8], but it can also be used for multi-bands under the circumstance in which bands can be summed up. The term $\frac{g(E)}{n(E)}$ is from the band, and the term $(1/\mu)(d\mu/dE)$ is from scattering. Therefore, the equation can be viewed as consisting of two terms that correspond exactly to two contributors to enhance α:

(i) increase the density of states (DOS) near Fermi level.

(ii) enhance the energy dependent scattering.

From Boltzmann equation, similar equation can be derived for σ:

$$\sigma = \int \sigma(E)(-\frac{\partial f_{eq}}{\partial E})dE \tag{1.17}$$

in which $\sigma(E)$ is the same differential conductivity as in the equation for α, and $-\frac{\partial f_{eq}}{\partial E}$ is the Fermi "window" factor. Since Fermi window factor narrow down the electrons contributing to transport property to those with energy close to Fermi level, thus a high value of $\sigma(E)$ within the Fermi window is necessary to increase the σ.
"Drude Model" gives σ a very straight forward explanation by relating the electron conducting ability to extrinsic parameters of the material:

$$\sigma = en\mu = ne^2\frac{\tau(E)}{m^*} \tag{1.18}$$

in which n is the carrier concentration, μ the mobility, τ the relaxation time and m^* the band effective mass. By increasing either the μ or τ by reducing the chance of charge carriers being scattered and increasing the time between consecutive scattering event, we can obtain a high σ.

1.3.2 Trade-off Between Electrical Conductivity and the Seebeck Coefficient

From the figure of merit equation $ZT = \frac{\sigma\alpha^2 T}{\kappa}$, we know that a high performance TE material needs to have high power factor (high α and σ), however, this is not the case in reality because α and σ are adversely dependent. This inter-dependency or trade-off can be easily explained using $\sigma(E)$ [9–11] as was introduced in section 1.3.1. When Fermi level is closer to the band edge, i.e. in a n type semiconductor, this means more states are becoming available above the Fermi level than below it. This cause the asymmetry of DOS with respect to Fermi level. If increasing the doping level in material to move Fermi level deeper into the band, σ could be increased. However, this also causes the $\sigma(E)$ to be more symmetric with respect to Fermi levels, which results in the decreasing of α.

This can be manifested in a more direct way. Fig. 1.8 shows the relation of carrier concentration with α and σ for metals and insulators. Between metal and insulator, with increasing carrier concentration α decreases exponentially, while σ increases from zero. However, the power factor $P(=\alpha^2\sigma)$ has a maximum at a certain value of the carrier concentration in the degenerate semiconductor region. Which indicating a narrow band gap can guarantee a relatively large σ while not sacrificing too much of α. The theoretical basis is originated from Sofo & Mahan's paper [12] in which the optimum band gap of thermoelectric materials is between 6 k_BT and 10 k_BT. And this range matches well the temperature for maximum ZT of some state of the art thermoelectric materials.

Besides being a degenerate narrow band gap semiconductor, other approaches such as quantum confinement [13] and energy filtering can also help to compromise the adversely dependent relation between α and σ.

1.4 Thermal transport in thermoelectric materials

The one parameter that describes how the heat is transported in the materials is called thermal conductivity κ. And usually, the heat can be transported by phonons (lattice vibrations), and thermalized electrons. Each mechanism contributes to the

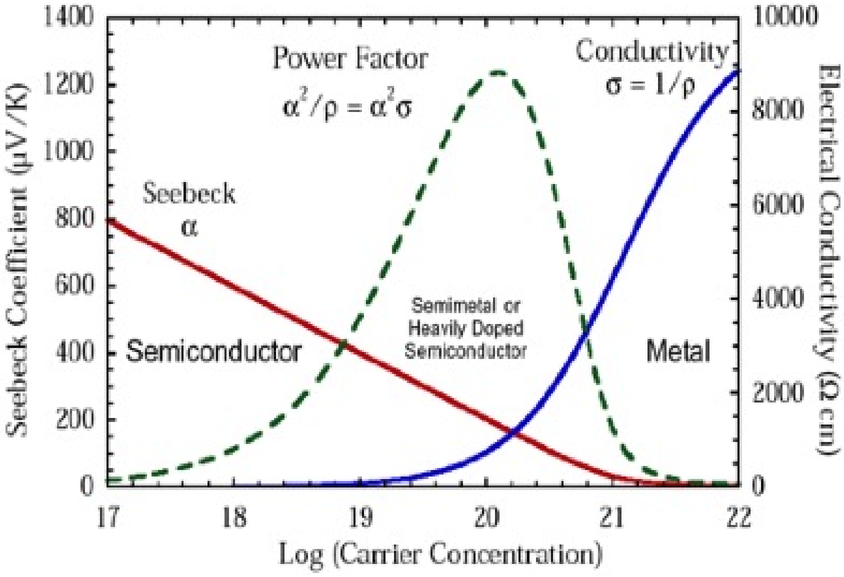

Figure 1.8: The optimization strategy for TE materials [14]

total thermal conductivity κ_T independently as seen in the following equation:

$$\kappa_T = \kappa_{ph} + \kappa_e \tag{1.19}$$

Where κ_e and κ_{ph} are the electrical thermal conductivity and lattice thermal conductivity respectively. Since only charge carriers in the conduction band participate in thermal transport, the electron contribution to the thermal conductivity κ_e is directly related to the σ through the Wiedemann-Franz relation:

$$\kappa_e = \sigma L_0 T \tag{1.20}$$

where T is the absolute temperature and L_0 is the Lorentz number: $2.44 \times 10^{-8} V^2 K^{-2}$ [15].

Besides the contribution of charge carriers, phonons' contribution to κ_T can be derived from kinetic theory [16]:

$$\kappa_{ph} = \frac{1}{3} C_v \upsilon L_{ph} \tag{1.21}$$

where C_v is the specific heat under constant volume, $L_{ph} = \upsilon\tau$ is the phonon mean free path (equals to velocity υ times relaxation time τ). Please refer to appendix C for the whole derivation of this equation.

Thermal conductivity is constrained mainly by four types of scattering: phonon-phonon (including normal process and umklapp process), electron-phonon, boundary, and impurity scattering of both electrons and phonons. Electron-electron scattering is also possible but weakly contributes to electrical and thermal conductivity due to the constraints imposed by the Pauli exclusion principle. All these types of scattering processes can take place in parallel and can be reflected in terms of their individual relaxation time τ. The summation that reflects their parallel relations is called Mathiessen's rule:

$$\frac{1}{\tau} = \frac{1}{\tau_{ph-ph}} + \frac{1}{\tau_{boundary}} + \frac{1}{\tau_{ph-el}} + \frac{1}{\tau_{impurity}} + \frac{1}{\tau_{el-el}} \tag{1.22}$$

This equation concludes that the most dominant scattering mechanism will be the one which has the shortest mean free path, or shortest relaxation time. However, Matthiessen's rule is not universally valid because individual scattering probabilities cannot be summed unless they are independent of one another.

It is worth mentioning that besides the four major scattering types that reduce thermal conductivity, "anharmonicity" is another scattering mechanism that is dominant in "cagey" materials to reduce thermal conductivity. This scattering mechanism applies in the Skutterudite materials in this work where guest atoms will be introduced

into the special "cages" with strong anharmonic potentials, resulting in off-center equilibrium positions for the guest atom to rattle around. So the rattlers in Skutterudite material can help effectively reduce thermal conductivity due to anharmonicity, which can be added into the Mathiessen's equation as another scattering term.
If explaining scattering mechanism of phonons in terms of its own property-wavelength, then it is generally true that a phonon is most effectively scattered by objects that are on the same length scale as its wavelength. Normally, impurities or boundaries that have only one length scale cannot efficiently scatter phonons. Therefore, a hierarchy structure with multi-length scales are preferred to scatter phonons and reduce thermal conductivity.

Although the thermal conductivity can be reduced by various scattering mechanisms as mentioned above, the scatter center would also have the possibility to scatter electrons. This is detrimental to electrical properties such as α and σ. Therefore, the challenge of optimizing these three ZT-governing TE properties σ,α and κ lies in the fact that these TE properties are inter-dependent. In this case, defect engineering is often used as an indispensable way to decouple these TE properties. While TE effect is a physical phenomenon existed in all materials, no TE material have attained its best performance without defects [17]. In the following chapter, how defects are closely related to these TE properties and how defect engineering can attain state-of-the-art TE performance will be introduced.

Chapter 2

Defect Engineering in the thermoelectric study

Throughout the entire six decades of modern TE research, the standard protocol would always follows the same procedure: first identify a promising parent compound among semiconductors or semimetals, then modify the crystal structure at multiple length scales to obtain the highest possible ZT. And defect engineering plays an important role in this protocol [17]. So what are defects? What is the defect engineering? The answers to these questions also explain the wide application of defects in high performance TE material.

By definition, any deviation from the perfect crystal is a defect. Since an ideal crystal is a highly symmetric geometric form, defects are created by symmetry breaking. Defects can also be regarded as the quasiparticles just like electrons, holes and phonons [17]. In this case, the whole thermoelectricity thus involves three types of quasi-particles: charges (electrons holes), phonons and defects. And the interactions between charges and defects, phonons and defects can tune the three TE properties $\{\sigma, \alpha, \kappa\}$ so as to decouple their inter-dependent relations in terms of tuning electron

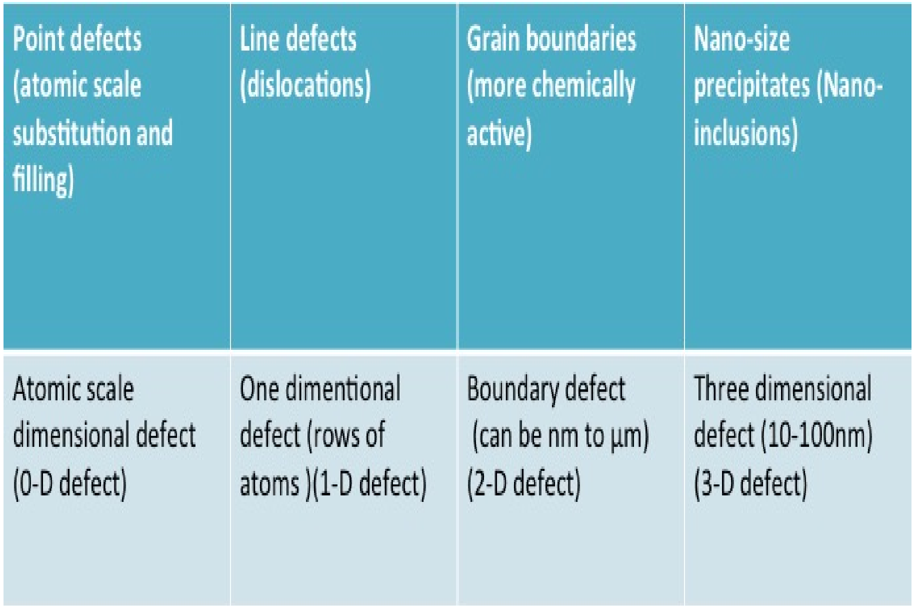

Point defects (atomic scale substitution and filling)	Line defects (dislocations)	Grain boundaries (more chemically active)	Nano-size precipitates (Nano-inclusions)
Atomic scale dimensional defect (0-D defect)	One dimentional defect (rows of atoms)(1-D defect)	Boundary defect (can be nm to µm) (2-D defect)	Three dimensional defect (10-100nm) (3-D defect)

Figure 2.1: Defects categorized by their dimensionality. From left to right, they are: 0-D defects: Point defects; 1-D defects: Dislocation; 2-D defects: Grain boundaries; 3-D defects: Secondary phases

and phonon density of states, or the electron and phonon scattering mechanisms. The design of what kind of defects or combination of defects to interact with other two quasi-particles (charges and phonons) so as to lead to a high TE performance can be regarded as the defects engineering.

Usually, defects can be categorized into various types based on their function, property or size. For the convenience of discussing defects in my project, I will categorize defects based on their dimensionality. As is shown in Figure 2.1. Since my project only involves 0,2 and 3-D defects in Co_4Sb_{12} skutterudites, I will only expand my discussion on these three types of defects.

1) 0-D defects. These are often known as point defects. And they can be further divided into extrinsic and intrinsic point defects. In filled Co_4Sb_{12} skutterudites, extrinsic point defects refer to dopants and fillers. They may enhance TE performance via optimizing the carrier concentration, reducing the thermal conductivity by scattering heat-carrying phonons, and in some special cases, enhancing the Seebeck coefficient by introducing resonant levels [18]. Meanwhile, the intrinsic point defects refer to vacancies that are either formed during material preparation, which occur at finite temperatures as a result of the competition between internal energy and entropy, or through intentionally designing.

2) 2-D defects. The most common 2-D defect is the grain boundary. 2-D defects can effectively scatter heat-carrying phonons to reduce the κ_{ph}, and also enhance the α via the electron energy filtering scenario. To attain high TE performance, grain boundaries should scatter phonons more effectively than charge carriers, and scatter those charge carriers with lower mean energy more effectively than those with higher mean energy. In filled Co_4Sb_{12} skutterudites with nano-inclusions, the interfaces exist between nano-inclusions and matrix can be regarded as multitude of grain boundaries. The different fermi levels on two sides of the boundaries can cause the scattering of lower energy electrons, so the electron energy filtering effect is more pronounced than in coarse-grained materials.

3) 3-D defects. These usually refer to secondary phases that can be implemented *in situ* or *ex situ*. The *ex situ* method usually requires mechanical mixing of host and secondary phase materials, while the *in situ* requires precipitation of secondary phases due to purposely going over the solubility or Filling Fraction Limit in filled Co_4Sb_{12} skutterudites. The 3-D defects usually co-exist with 2-D defects that can help increase the Seebeck coefficient by electron energy filtering [19] and decrease lattice thermal conductivity due to scattering phonons with comparative length.

Although these defects are categorized based on their own characters, they can interact with each other. i.e., one type of defects can lead to the formation of another type of defects. A good platform to study how defects interact to affect the TE properties would be Skutterudites - one of the state of the art thermoelectrica materials, which is also the focus of this thesis.

Chapter 3

Skutterudite Thermoelectrics

Since the concept of "phonon glass electron crystal"(PGEC) has been introduced by Slack to realize high performance thermoelectric material. Skutterudites have obtained much attention for the point of view of PGEC considering they usually have very good electrical properties due to a narrow band gap($\sim$ 0.2eV). One of the typical skutterudite compounds Co_4Sb_{12} have large power factor in a temperature region 600-800 K and have already been used in real life as thermoelectric devices for power generation.

3.1 Skutterudite crystal structure,band structure and thermoelectric properties

3.1.1 Crystal structure of Skutterudite

Skutterudites - whose name originated from a mining town, Skutterud, in Norway by Oftedal in 1928 [20, 21]. It is usually depicted in the binary compounds form of composition MX_3(M: transition metals, such as Co,Fe,Rh or Ir. X: pnicogen atoms,

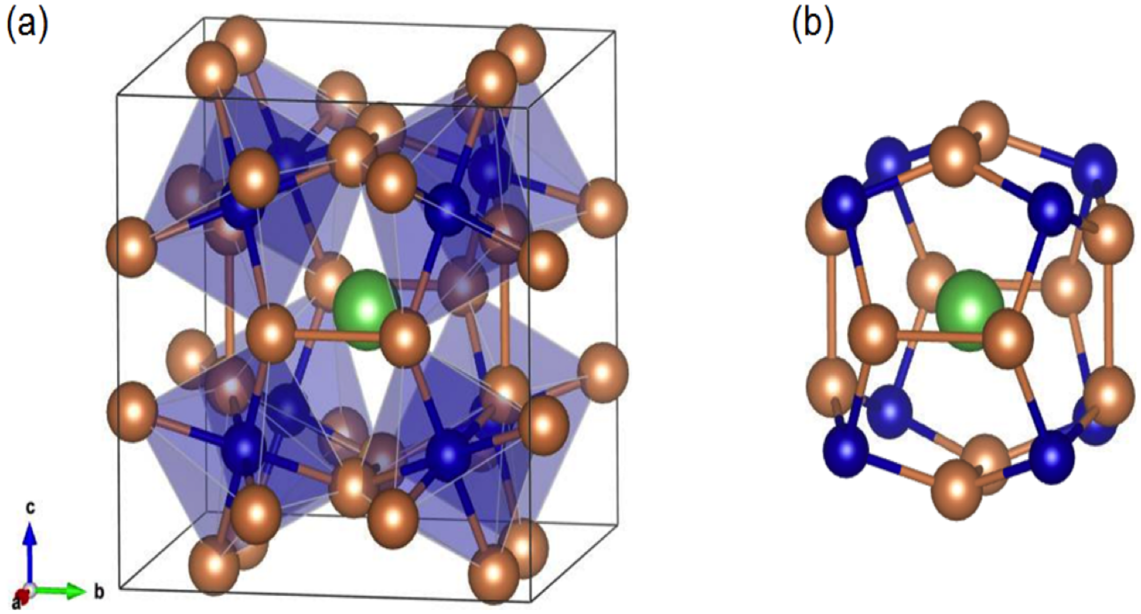

Figure 3.1: Body-centered cubic crystal structure of $CoSb_3$ skutterudite with a net work of corner-sharing octahedra (a) and with a guest atom filled into the dodecahedron cage (b). Transition metals (M), pnictogens (X), and fillers are in blue, yellow and green, respectively.

such as P, As or Sb) with a complex body-centered structure belonging to the space group $I_m\bar{3}$. The unit cell contains eight structures with formula MX_3 (as shown in Fig. 3.1(a)), the eight M atoms is at c position and the twenty four X atoms occupy the g position. The X_4^{4-} ring formed by four M atoms centered in the cubic structure formed by eight M atoms. The structure of Skutterudites is usually presented in the form of $\Box M_4X_{12}$ which contains only one half of the unit cell (The box represents the voids, shown in Fig. 3.1b) that highlights the presence of its single void $\Box$ and X_4 planar,rectangular four-membered rings of pnicogen atoms. Filled skutterudites ($R_yM_4X_{12}$, R is the filling element) are obtained by fully filling or partially filling the voids.

3.1.2 Band structure of Skutterudite

The electronic structure of Co_4Sb_{12} has been thoroughly studied over the last decade [22] using Density Functional Theory (DFT) by different research groups and scientists. In order to validate our calculation of the electronic structure of $CoSb_3$ before addressing more complex filled $CoSb_3$ skutterudites problems, a careful comparison of our calculation with others' is necessary.

The 2×2×2 bcc supercell of $Co_{32}Sb_{96}$ which contains eight dodecahedron voids were examined. The band structure and density of states (DOS) of $Co_{32}Sb_{96}$ are shown in Fig. 3.2. Our result is comparable to that of Snyder and colleagues calculated for the same 2×2×2 bcc supercell, except for the small difference in the band gap [23]. As can be seen from the band structure in Fig. 3.2(a), there is a direct band gap of 0.23 eV at the Γ point between the valence band maximum (VBM) and the conduction band minimum (CBM). This value is comparable to the LDA and PBE results of 0.22 and 0.17 eV by Sofo *et al* [22] and is also within the LDA range of 0.195-0.330 eV depending on the lattice constant calculated by Lefebvre-Devos *et al* [24]. Even with quasiparticle GW approach, the band gap is only increased to 0.335 eV [25]. Hammerschmidt *et al.* conducted a systematic study using various exchange correlation functionals and found a band gap dependence on the applied functionals, which may affect the band gap by the optimized lattice constant and the amount of Hartree-Fock exchange included [26]. On the other hand, the DOS shows an indirect pseudogap of 0.57 eV between the first peak of valence DOS located at -0.34 eV below the VBM and the tiny conduction DOS peak corresponding to the CBM. This value is the same as the theoretical result of Singh and Pickett [27] and agrees with the experimental estimation of 0.5 eV via high temperature electrical resistivity measurement by Dudkin and Abrilosov [28]. Caillat *et al.* and Nolas *et al.* also reported experimental band gap of 0.55 eV by transport property and Hall probe measurement [29,30]. Note that the wide range of band gap values in the literature [31,32] may indicate the necessity to differentiate between the direct band gap and the indirect pseudogap. Further based on the partial DOS analysis (Fig. 2a), it can be seen that the first valence DOS peak at -0.34 eV below the VBM consists of the hybridization from Co's and Sb's p states, whereas the tiny conduction DOS peak corresponding to the CBM is dominated mainly by Co's states, largely agreeing with the observation of Zhao *et al.* for the same $Co_{32}Sb_{96}$ supercell [33].

Singh and Pickett uncovered a remarkable feature in the band structure of pristine skutterudites [27], i.e., a single valence band crossing the psuedogap shows largely a quasilinear dispersion except for a quadratic shape in a narrow region near the zone center. Smith *et al.* recently put forth a theoretical model showing that this quasilinear gap-crossing band is in fact associated with the massless Dirac bands similar to the case of graphene. By varying the Sb atomic coordinates, they revealed a critical point along the transformation path from perovskite toward skutterudite where the two massless Dirac bands touch each other and meanwhile are degenerate with two other massive conduction bands. Accordingly, the Fermi surface becomes just a topological point at the zone center. Simply by a small structural deviation from the critical point, the four-fold degeneracy is lifted yielding a small direct band gap at the Γ point. Since the mineral skutterudite is very near the critical point in its natural state, the direct gap is found to be small and highly sensitive to the atomic positions of the Sb atom [22, 34]. As can be seen from the band structure, the quasilinear valence band symmetrically flanks the Γ point and features a large dispersion. The slope is +3.03 and -3.02 eV$\mathring{A}$ in the Γ-N and Γ-P zone, respectively. Three conduction bands siting right above it are triply degenerate at the Γ point but diverge immediately into three separate bands along the Γ-N direction and also into a pair of doubly degenerate bands at a lower energy and a singly degenerate band at a higher energy along the Γ-P direction. It is noteworthy that, unlike the lower two massive bands which are quadratic, the third higher conduction band mirrors the gap-crossing valence band in relation to the massless Dirac bands. The slope is -3.03 and +2.96 eV$\mathring{A}$ in the Γ-N and Γ-P zone, respectively, close to that of its valence counterpart. By turning on SOC effect for the primitive bcc cell of Co_4Sb_{12}, the degeneracy of the three conduction bands are lifted, except for the lower two bands at the Γ point. The lower two conduction bands are the heavy-electron and light-electron band, respectively, while the third is a split-off band lying only 0.02 eV above the other two at the Γ point, which is still quasilinear with SOC applied. In addition, the direct band gap at the Γ point is reduced only slightly to 0.18 eV. From the small SOC effect shown herein for the primitive lattice Co_4Sb_{12} and in the literature for compositionally similar $LaRu_4X_{12}$ (X=P, As, Sb) skutterudites [35], it appears unnecessary to apply SOC toward the electronic structure calculations of the La-filled systems.

3.2 Research advances of Skutterudites

For Skutterudite materials that have already had good electrical properties (high power factor $\sigma\alpha^2$), especially for $CoSb_3$ skutterudites, lowering their thermal conductivity has become the focus. And the lattice thermal conductivity takes a large portion of the total thermal conductivity, therefore, improving the TE properties of $CoSb_3$ Skutterudites count on lowering the lattice thermal conductivity. In the following sections, we will address how defects were used to decrease the lattice thermal conductivity in $CoSb_3$ skutterudites in TE material research history as well as how defects engineering is implemented.

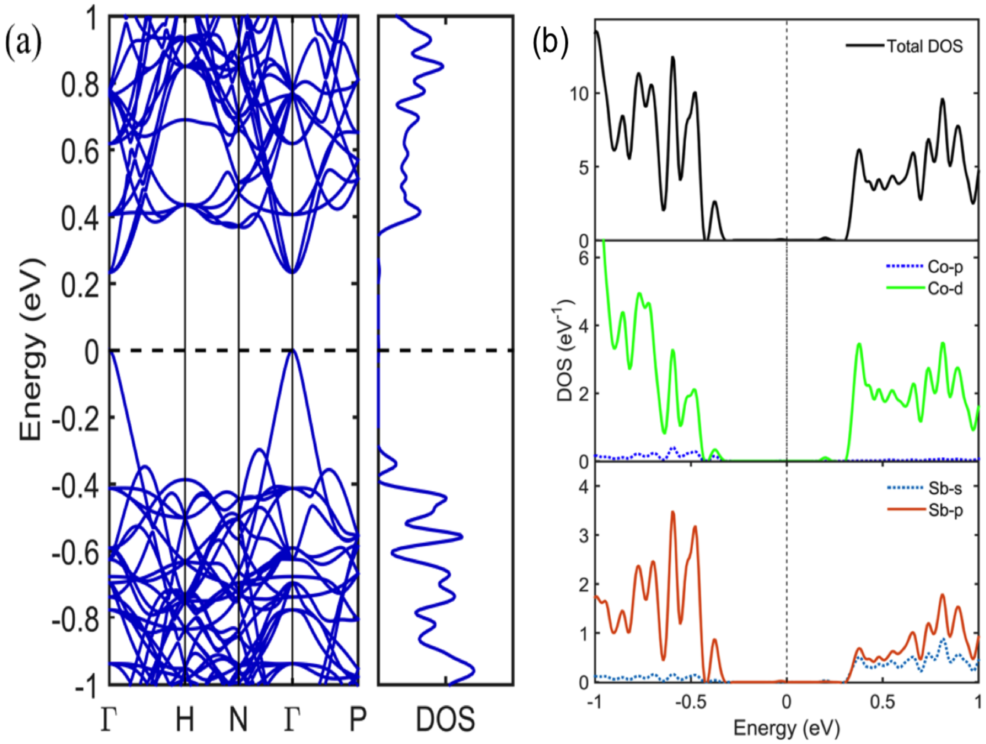

Figure 3.2: (a) Band structures and total density of states (DOS) for $Co_{32}Sb_{96}$. (b) Total and partial density of states (DOS) for $Co_{32}Sb_{96}$.

3.2.1 Introduction of 0-D defects in $\mathrm{CoSb_3}$ skutterudites

1) Substitutionally doped Skutterudites. Ioffe brought up an observation in 1957 in one of his publications that *heavily doped semiconductors make the best thermoelectrics*. The most conventional and effective way to decrease the lattice thermal conductivity of Skutterudites is through substitutional doping (0-D defect).The doping in $\mathrm{CoSb_3}$ skutterudites is often heter-electronic doping on either Co site or Sb site. Co can usually be doped by Fe and Ni; Sb can usually be doped by Ge,Se,Sn and Te to form ternary compound or multicomponent compound. The principle of doping is to increase the scattering of phonons by point defects and optimize the carrier concentration so as to improve TE properties. [36, 37].The earliest research of $\mathrm{CoSb_3}$ focused most on doping on the Co site. The Jet Propulsion Laboratory studied the TE properties of p-type $\mathrm{Ir_xCo_{1-x}Sb_3}$ alloys, the results showed that when x=0.88, its lattice thermal conductivity can be decreased by 70% compared with the corresponding binary alloy, and the ZT can reach 0.5 around 700 K.

2) Filled Skutterudites and Filling fraction limit. Filled Skutterudites is from filling the Sb icosahedron void with guest atoms [20, 38–41]. The alien atoms can benefit TE properties in following two aspects: First, the phonons can be strongly scattered by the "rattling" effect from the alien atoms connecting weakly with the surrounding atoms due to their small ionic radius and rattling among multiple potential minima positions in the cage, so the lattice thermal conductivity can be greatly decreased. We can also call this alien atom "rattler" in this case. Second, the filling atom can help adjust and optimize the carrier character and electrical properties. Recently, more work showed that [37, 41–44] the rare earth elements (La, Ce, Pr, Eu *et al.*) with a small ionic radius and a large atomic mass can help lower the lattice thermal conductivity when they are filled into the voids as alien atoms; and some alkaline elements with low oxidization valence (Ba, Sr, Ca) can help improve the electronic properties when filled into the naturally formed voids.

The most frequently studied filling atoms are from Lanthanum and alkaline earth metal, such as La, Ce, Ca, Ba *et al.* In 1996, Sales *et al.* reported a ZT value ≈ 1.4 in filled skutterudites, which makes Skutterudites the one of the most promising TE materials in mid-temperature range. Shanghi Institute of Ceramics synthesized *p*-type $Ce_{0.28}Fe_{1.52}Co_{2.48}Sb_{12}$ having a ZT value of 1.1, η_{max} can reach above 8%. However, the nano-sized icosahedron void can not be filled infinitely. Shi *et al.* [45] studied the filling fraction limit (FFL) of $CoSb_3$ skutterudite by density functional thoery (DFT) method. The FFL is shown to be determined not only by the interaction between the impurity and host atoms but also by the formation of secondary phases between the impurity atoms and one of the host atoms. The predicted FFLs for Ca, Sr, Ba, La, Ce, and Yb in $CoSb_3$ skutterudite are in good agreement with reported experimental data. Fig. 3.3 [45] presents a list of filling elements and their FFLs, which has played an important role in guiding the optimization strategy for TE properties.

Yang *et al.* [45, 46] used phonon resonance scattering mechanism to simulate the phonon interactions in a qusi-local thermodynamic environment. Their study showed that this scattering mechanism can effectively decrease the lattice thermal conductivity in Skutterudites. They further proved the existence of this scattering mechanism experimentally using inelastic neutron scattering. In this system, the interactions between lattice phonons and localized low frequency phonons can produce some bound states (resonant states) [45], these resonant states will bound certain phonons and discrete their wave vectors so as to increase the intensity of phonon scatterings. The study on phonon resonance scattering also showed that only the phonons that have the same frequencies as the localized vibration spot can be scattered this way. Therefore,

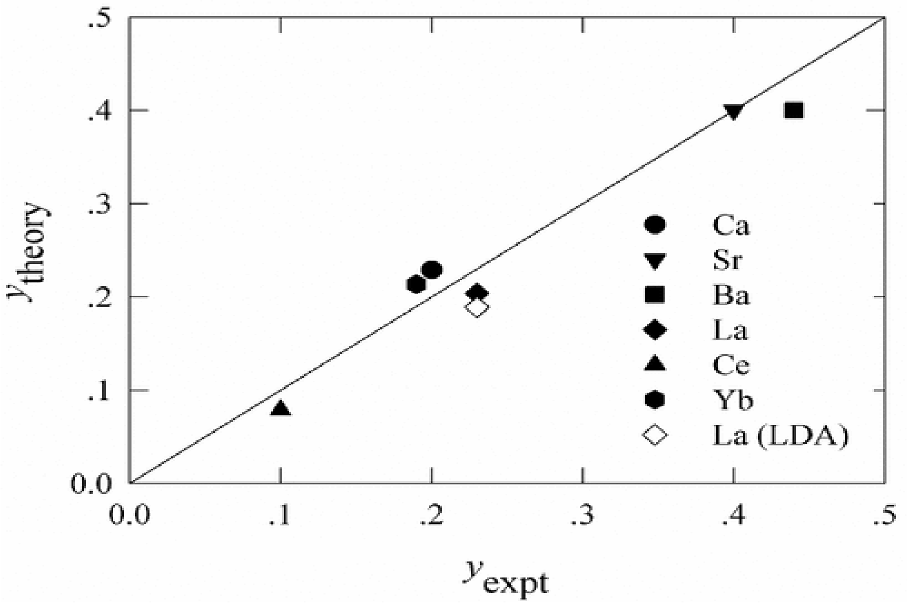

Figure 3.3: Calculated filling fraction limits (FFLs,y_{theory})vs the experimentally measured FFLs (y_{expt}). The solid line represents $y_{theory} = y_{expt}$ [45].

if some structure can provide localized vibration modes such as filling the Sb icosahedron voids with multiple atoms with different vibration frequencies to wider the distribution of localized vibration frequency range, then theoretically more phonons in the lattice can be scattered. This prediction lay the path for double-filled and triple-filled Skutterudites. In 2008, based on this theoretical guidance, Shi *et al.* [47] synthesized a series of n type Ba and Yb double filled $Ba_xYb_yCo_4Sb_{12}$ compounds, the TE property measurements showed a much lower lattice thermal conductivity than single-filled Skutterudites, and much better TE properties over the entire temperature range studied. Among these series of of samples, $Ba_{0.08}Yb_{0.09}Co_4Sb_{12}$ have a ZT value of 1.36 at 800K, which was the best among all the Skutterudite materials at that time. Also, Zhao *et al.* [48] reported that Ba, In double filled $Ba_{0.14}In_{0.23}Co_4Sb_{12}$ have a ZT of 1.34 at 850K. All these reports showed that double filled Skutterudites can further improve the electronic properties, decrease the lattice thermal conductivity. This is the reason for the extensive study of multiple filled Skutterudites recently, and also why single filling is less heeded.

3.2.2 implementation of 3-D defects in $\mathrm{CoSb_3}$ skutterudites

Nanocomposite. The thermoelectric nanocomposite, a new paradim for high performance thermoelectrics, consistently attain even greater ZT. The thermal conductivity of the composites is suppressed significantly by nanosized secondary phases (nanoinclusions), well-dispersed within a host matrix. The nanoinclusions with dimensions smaller than the phonon mean free path and with maximum interface density, can usually significantly scatter heat-carrying phonons, retarding the lattice thermal conductivity dramatically. To avoid diminished electrical conductivity, however, they must also be larger than the charge-carrier mean free path in order to minimize adverse carrier scattering. In addition, analogous to filled skutterudites, nanoinclusions may also increase the power factor ($\alpha^2\sigma$): the α and σ may be enhanced by energy filtering and modulated carrier doping, respectively [49–51].

Consequently, many promising skutterudite-based nanocomposites with large ZT have been reported [52, 53], the most notable (achieving ZT up to 1.43) consisting of nanoinclusions reportedly synthesized *in situ*. However, the origin of the nanoinclusion materials- originating from either impurity phases of meta-stably filled void, which means the guest atom is thermodynamically unstable in the void sites-was not definitively determined. In this thesis, although the nanoinclusions were introduced *in situ* by intentionally passing the FFL, the possibility that nanoinclusions were formed way before over the FFL can not be excluded.

Chapter 4

Research goal and strategy

This dissertation project began with interest in the roles of a single filler in skutterudite system. Since the study trend has been shifted to multiple filled skutterudites so fast, single filled skutterudites has scarcely been studied due to its low efficiency. However, to reveal the physics behind the filling behavior- what is the physical identity of the guest atom? Be a normal filler or a rattler- requires us to go back to the most fundamental case-single filled case. To this end, La was chosen as the guest atom based on two reasons: 1) Rare earth elements were customarily thought to be good rattlers, by studying La, the first element in rare earth group, we can reveal the "roles" of La as a guest atom (rattler or filler). 2) La, as the first element in rare earth group, dose not have *f* electrons, which ensures more feasible and trustful DFT calculation results. We started with experimentally preparing a series of La filled Co_4Sb_{12} samples with various La compositions ranging from below the FFL to above the FFL. Sb deficiencies occurred during the preparation of the sample due to a high vapor pressure, thus we had a Sb-vacancy doped Co_4Sb_{12}. Also, La-Sb nano-sized secondary phase precipitated when La content was over the FFL, and the formation of La-Sb secondary phases would also induce Sb vancancies. With this filling-doping-nanocomposite method, we've discovered that by using only one control parameter, the ZT can improve largely compared with the pristine sample. However, the experimental results cannot unequivocally indicate the physical identity of the guest atom, nor explaining the cause of the dramatic σ change with the occurrence of the La-Sb secondary phases. Hence, studying the La filled Co_4Sb_{12} theoretically using DFT, and exploring the role of La became the main goal in this dissertation.

We started the DFT calculations with two different La filling conditions (12.5 *at*% and 25 *at*%) in Co_4Sb_{12} matrix. As a result, the electron band structure, density of states(DOS), charge density plots were all calculated. The impact of La addition and Sb deficiencies on band structure were explored. Calculated result acted as a good support on experimental result. In summary the thermoelectric study combining with the DFT calculations helped us study the defects chemistry (how point defects including Sb vacancies and La fillers interact with nanocomposite), and how their interplay influence the thermoelectric properties, which may shed some light on other single filled or multiple filled Skutterudites.

Chapter 5

Experimental procedures and theoretical calculations

5.1 Synthesis procedures

5.1.1 Synthesis

The melting-annealing-sintering method was used to synthesize the sample. Stoichiometric amount of Cobalt (Co) powder (99.998%; Alfa Aesar), Antimony (Sb) powder (99.9999%; Alfa Aesar®) and Lanthanum (La) Powder (99.998%; Alfa Aesar) were mixed thoroughly according to each sample's compositions. The nominal compositions are $La_yCo_4Sb_{12}$ (y=0.1,0.2,0.3,0.4 and 0.6). Admixtures were then placed into a quartz tube with a piece of quartz wool in the glove box with protection gas. The quartz wool was used to prevent powders to be sucked into the vacuum system. Then the quartz tube was evacuated and sealed under high vacuum. Samples were then placed in a Carbolite® model CWF 13/23 box furnace for the melting and annealing process. The furnace was heated to 874K, adwelt for 3 hours, then heated to 1323K

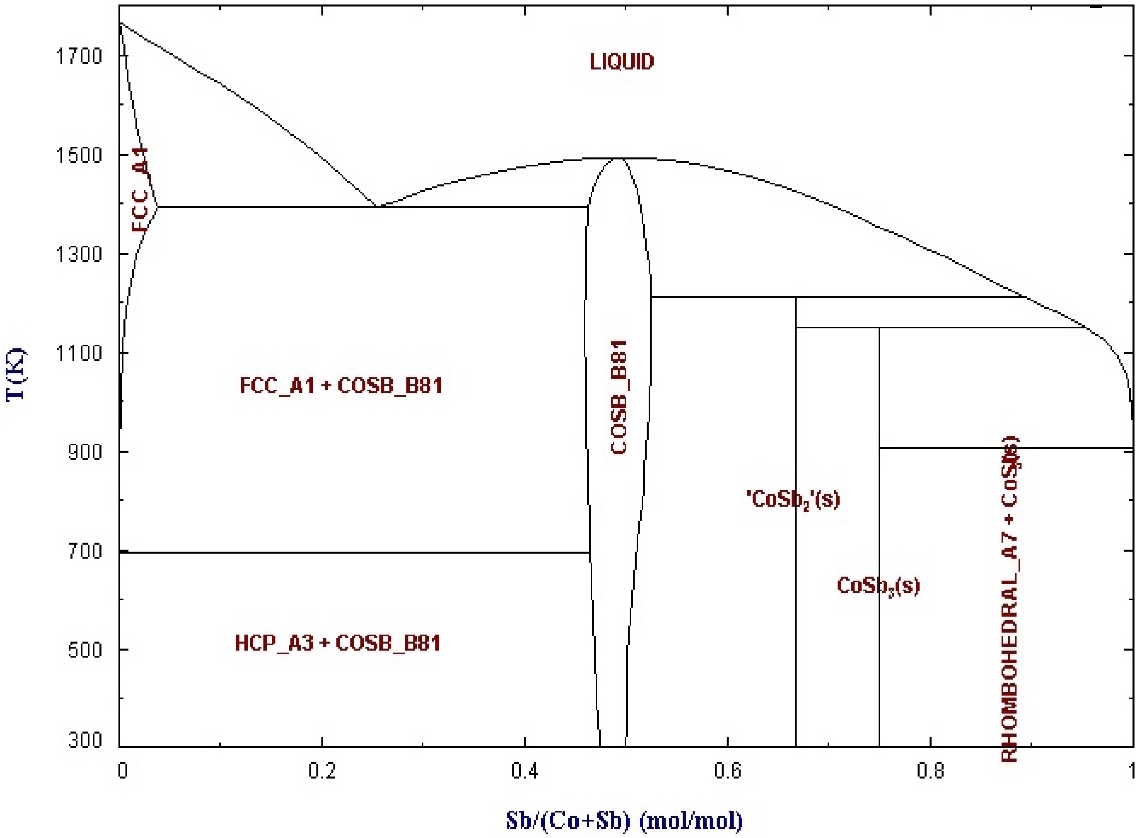

Figure 5.1: The binary phase diagram of Co-Sb [54].

and held for approximately 30 mins to ensure the homogeneity of the melts. Then the furnace was cooled to 923 K within 45 minutes and held for 72 hours (see Fig. 5.1 for the phase diagram [54]). After furnace cool the solid in the quartz tube was then grinded into powder and sintered into a compact disc using Spark Plasma Sintering (SPS) for characterization.

5.1.2 Spark Plasma Sintering

Spark Plasma Sintering (SPS) is a sintering process that make the densification possible in a short period of time by sparking or plasma generation [55]. The large spark pulse current flow through the graphite mold and stacked powder can consolidate a

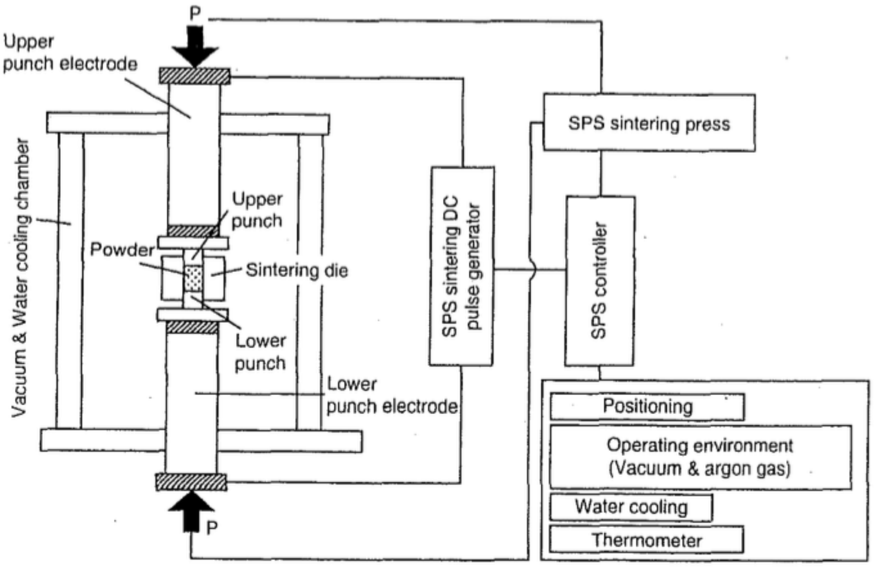

Figure 5.2: Schematic diagram of Spark Plasma sintering device [56].

homogeneous, high quality sintered compact due to the uniform heating, surface purification and activation made possible by dispersing the spark points [56]. Moreover, the fast cooling rate of the sample and the graphite mold after the pulsed current is cut off can be as fast as 300 K/min, therefore, the whole sintering process can usually be done in about 15 minutes. Fig. 5.2 [56] presents the basic configuration of the SPS system. The system consists of a SPS sintering machine with a vertical single-axis pressurization mechanism, two punch electrodes with built-in water cooler, a water-cooled vacuum chamber, a vacuum/air/argon-gas atmosphere control mechanism, a cooling water control unit, a position measuring unit, a special DC-pulse sintering power generator, an applied pressure display unit and other interlock safety unites. In our experiments, a Dr. Sinter Lab, SPS-515S SPS system was used. All samples were pulverized into powders with a mortar and pestle from the melt process described above. The powders was then placed into a 12.7 mm diameter graphite die with graphite foil in between the powder and graphite punches for the ease of removal after sintering and a more uniform current flow. The graphite die was then placed in between graphite spacers with a thermocouple placed in a hole on the side of the die to measure the temperature of the powder during the sintering. After setting up the place for the graphite die, the chamber was closed and the furnace was purged and backfilled with Argon three times to ensure a vacuum environment before sintering. After applying the heating program, the whole process took about 20 minutes. The pressure was held at at constant 6.0 kN with DC on:off pulsed of 12:2 units (each unit=2.8 msecs). The finalized sintered discs would have a 12.7 mm in diameter and $\approx$ 2-3 mm in thickness.

5.2 TE property measurements

Restricted by the different working temperature range of measuring equipment, all measurements were conducted both in high temperature (above 300 K) and low temperature (below 300 K) using different apparatuses.

5.2.1 Thermal conductivity measurements

The SPSed samples were in diameter (12.7 mm) that was made specifically for thermal diffusivity measurement. Before the measurements the disc were coated with a dfg 123 graphite spray for a thin coat of graphite to ensure good thermal homogeneity when the sample is heated, good absorption of the pulsed laser input and IR detection for the temperature. The disc is then placed in SiC sample holder and Nezstch® Microflash 457 transient technique system for high temperature thermal diffusivity measurement. Fig. 5.3 shows the basic configuration of the LFA system.

After purging and back-filling with Argon several times, the system was left with a continuous Argon purge at a flow rate of 75 mL/min before measurement. Sample

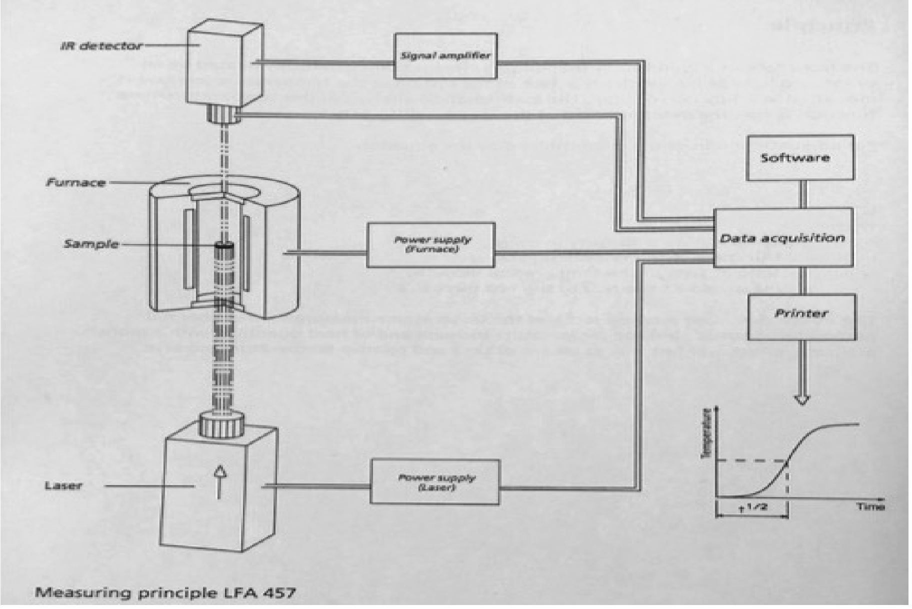

Figure 5.3: The basic configuration of Nezstch® Microflash 457 transient technique system for high temperature thermal diffusivity measurement [57].

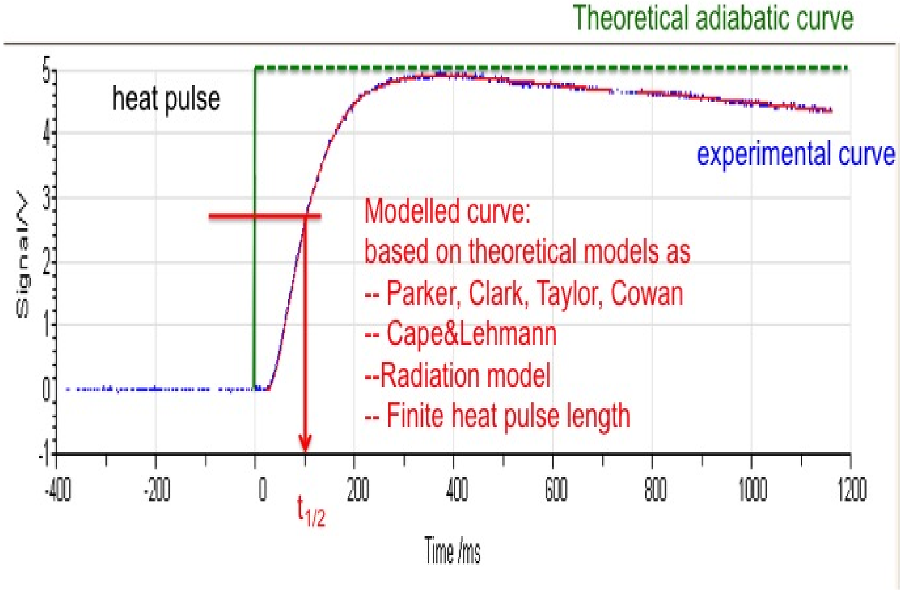

Figure 5.4: The temperature vs time curve for fitting. The theorectical models [58–60] in the graph were used to fit the experimental result [57].

temperature was measured by an S type (Pt:Pt-Rh) thermocouple. While the temperature and baseline was stabilized, a Nd-glass laser was charged and activated to heat the bottom of the sample. The heat transfer through the sample was detected by a liquid nitrogen cooled Indium Antimonide (InSb) infared detector. Temperature vs time is plotted as shown in Fig. 5.4. If the width of the laser pulse is infinitely small or negligible compared with the sample temperature raising half time, the transfer of heat in the sample can be simply regarded as one dimensional heat transferring from top surface to bottom surface without horizontal heat loss through side. And if adiabatic conditions apply to the environment (that is to say the temperature of the bottom surface will raise to the maximum point and stay), then we can calculate the thermal diffusivity through the temperature raising half time $t_{1/2}$(the time it takes for the bottom surface to raise the temperature half of the maximum temperature) and the sample thickness d:

$$D = 0.1388\frac{d^2}{t_{1/2}} \tag{5.1}$$

For the bulk sample we measured, Cowan+Pulse model [58] was used to fit the temperature rising curve, if fits well, the Netzsch LFA Measurement v. 4.8.0 software can read a value for thermal diffusivity. Then at each temperature point, this whole process above is repeated. The average thermal conductivity is related to thermal diffusivity in following equation:

$$\kappa = C_p \rho_d D \tag{5.2}$$

Where ρ_d is the density and C_p is the heat capacity at constant pressure. The density was calculated using the Archimedes method. In practice, C_p can be measured by differential scanning calorimetry (DSC), however, in the case of skutterudite materials that function at mid temperature (300 K to 800 K) range, all phonons will be excited in which a Dulong Petit limit ($C_p \approx 3R$) can be used to estimate C_p. Therefore, the thermal conductivity values were then calculated for the entire temperature range measured (50 C° -475 C°).

For low temperature thermal conductivity measurement, a steady-state custom designed technique was used. Samples were cut into 2×3×8 mm^3 bars with a larger cross section to lessen the radiation by reducing the surface to volume ratio. Two samples were mounted to pucks modified from a Quantum Design Physical Properties Measurement System (QD® PPMS) pucks (Fig. 5.5 [6]). The details of this custom designed thermal conductivity system is described elsewhere [61]. The sample pucks were then placed inside the custom designed low temperature κ measurement system. Three separate radiation shields were placed over the sample to minimize any radiation loss. The system was then purged to $\approx 10^{-5}$ torr using a Leybold® Turbotronik NT 151/361 turbo pump. After inputting the sample dimensions in the system, the system was then cooled using a cryocooler, APD®Displex Close Cycle model CSW-202N cryostat with helium compressor. Measurements were then taken during warming from 10 K to 300 K. The steady state method of this low temperature κ measurement performs a power P vs ΔT sweep at constant temperature across the sample using a constant current source measuring the resulting resistance and calculating the power output from the equation

$$P = I^2 R - P_{loss} \tag{5.3}$$

where P_{loss} is the power loss due to radiation at room temperature. The system software then used the slope of P vs ΔT to calculate the over κ, including looses,

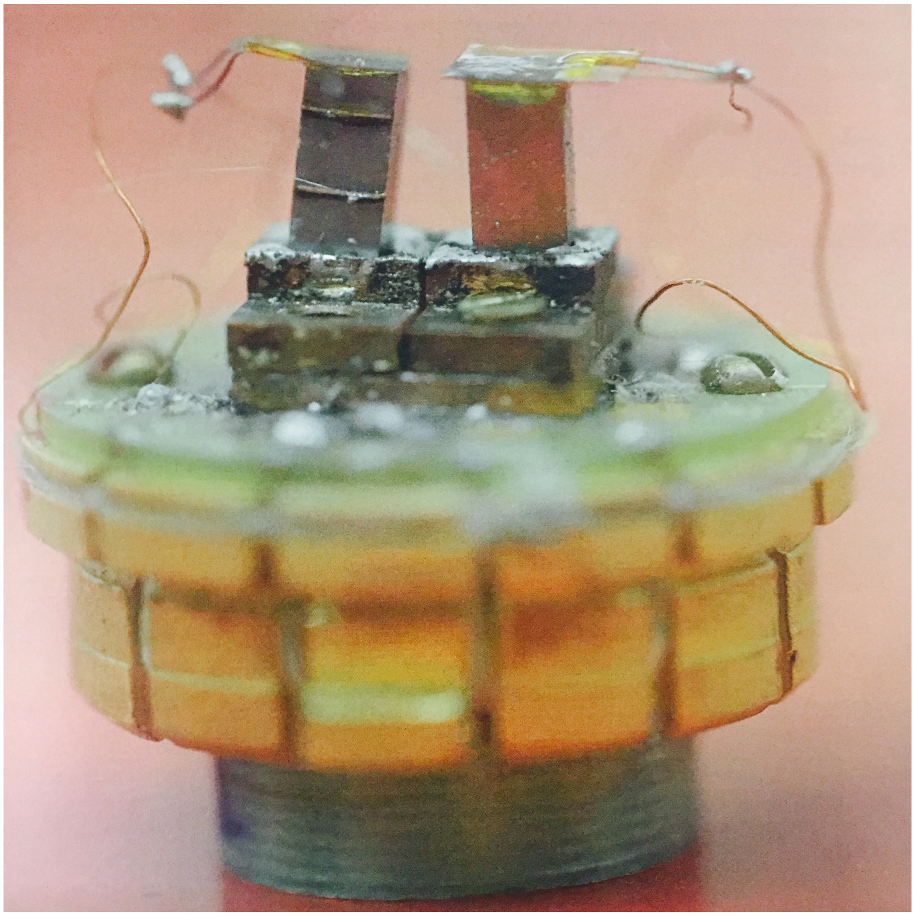

Figure 5.5: QD-PPMS® modified mounted puck for low temperature thermal conductivity measurement [6].

using the equation,

$$\kappa = \frac{PL_0}{A\Delta T} \tag{5.4}$$

where L_0 is the temperature difference between the leads and A is the cross-sectional area of the sample.

To remove the radiation affects on the near room temperature κ data, a radiation correction fitting was used. The power radiated from the sample included in the P_{loss} term above is given by Stefan-Boltzmann law

$$P_{loss} = A_s \vartheta \epsilon (T_b^4 - T_s^4) \tag{5.5}$$

where A_s is the surface area and ϑ is is the Stefan-Boltzmann constant, ϵ is the emissivity. T_b is the base temperature and T_s is the sample temperature, and

$$T_s = T_b + \Delta T \tag{5.6}$$

For mathematical simplicity, using the Taylor expansion, we will have

$$P_{loss} \propto T^3 \tag{5.7}$$

which has been simplified by using Taylor expansion. And after applying this T^3 fit to the κ above about 200 K, it can help to correct the near room temperature κ to match the high temperature κ.

5.2.2 Seebeck coefficient and Electrical conductivity measurements

The seebeck coefficient and electrical conductivity were measured simultaneously both in high and low temperature measurement. After high temperature thermal conductivity measurements, the disc shape samples were cut into $13 \times 2 \times 3 mm^3$ bars for high temperature electrical resistivity ρ and Seebeck coefficient α measurements. Sample dimensions were measured using a Vernier® caliper and entered into the measurement system ZEM 35.0 for HT SDC 35 software, along with desired temperature program, and ΔT between thermocouple probes. Measurement were taken from room temperature to approximately 475 C° using the Ulvac® systems 4-probe method with two spring loaded thermocouples, on the side of the sample, and two spring loaded ceramic arms, allowing for thermal expansions, with Ni electrodes holding the sample in place. Distances between the two thermocouple probles were measured using a DinoLite® camera and DinoCapture 2.0 v. 1.4.3 software. Two slics of Nickel foil were used in between top and bottom Ni electrodes and sample faces to ensure the best electrical contact. Before measurements, sample was tested for reliable electrical contacts using a measurement plotting voltage vs current to make sure a linear resistance and thus a good Ohmic contact. After this, a Ni radiation shield was used to cover the sample for eliminating thermal noise due to radiation effects. The system was then purged and back-filled with high purity helium gas three consecutive times with 10 minutes intervals between each purge and fill. The resistivity of the sample ρ was measured using the equation

$$\rho = \frac{l}{A} R \tag{5.8}$$

in which A is the cross-section area calculated from the measured thickness and width of the sample, l is the measured distance between the two thermocouple probes, R is the measured resistance. Seebeck coefficient α measurement use the equation

$$\alpha_{AB} = \frac{\Delta V}{\Delta T} \tag{5.9}$$

where the ΔV and ΔT are measurable quantities that are not reliant on sample dimensions. Samples were measured at every 50 C° with ΔT intervals of 5,10 and 1.

Low temperature resistivity and Seebeck coefficient were measured using $2 \times 3 \times 12 mm^3$ bars still cut from the disc. The sample bar was then mounted on a custom designed sample puck, as is shown in Fig. 5.6 [6]. And the two parameters (α and σ) were measured semi-simultaneously on each sample using four probe method during cooling and warming. Samples were cooled from 300 K to 10 K at a rate of 0.75 K/min using a ΔT between the two ends of the sample of 5 K. At each temperature point, current was pulsed for $\approx$ 100 ms while reading the voltage from the voltage leads on the sample. The current pulsed was first run through the 10 Ω standard resistor for accuracy of current measurement.

5.2.3 Susceptibility measurements

Due to the special property of our sample, we need to measure susceptibility to approximate the carrier concentration. Magnetic susceptibility are calculated from the Q-D PPMS® system using a Vibrating Sample Magnetometer (VSM). The VSM applies sinusoidal vibrations to the sample. A few mg of powder were placed inside a cylindrical snap-in capsule sample holder with the powders centered as closely as possible to the 35mm mark (Fig. 5.7 [6]). The snap-in capsule is then placed in a

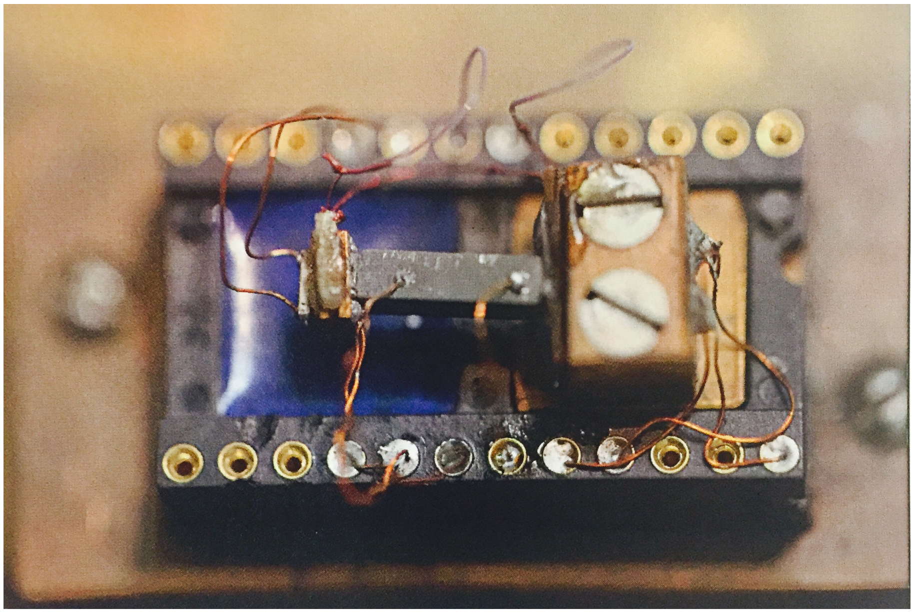

Figure 5.6: Completely mounted low temperature resistivity and Seebeck coefficient measurement puck [6].

pick-up arm and placed inside the QD-PPMS® system for measurement. Samples were measured using a temperature program. A steady + 5000 Oe magnetic field is applied the sample and the resulting magnetic moment (M) is measured via the induced voltage in the pick-up coil surrounding the sample (Fig. 5.8 [6]). And then the measured magnetic moment from the VSM can be divided by the measured mass of the powders. Therefore, the mass susceptibility can be calculated via the magnetic field and the moment per unit mass. The mass susceptibility can be converted to moles giving the molar susceptibility, which indicates the degree of magnetization of a material in response to an applied magnetic field.

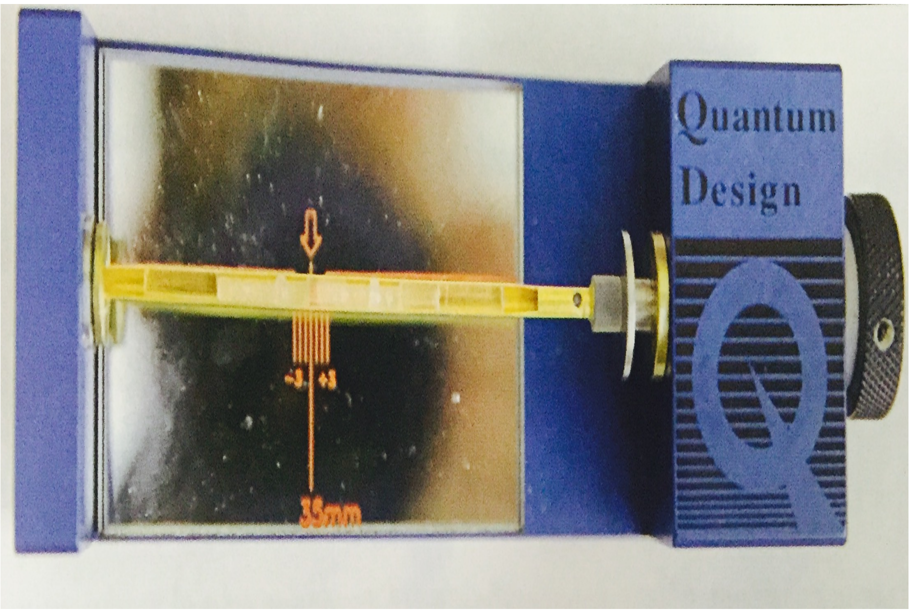

Figure 5.7: Bronze trough with 35 mm mark to accurately center the sample in the sample holder for balancing and thus accuracy of measurement [6].

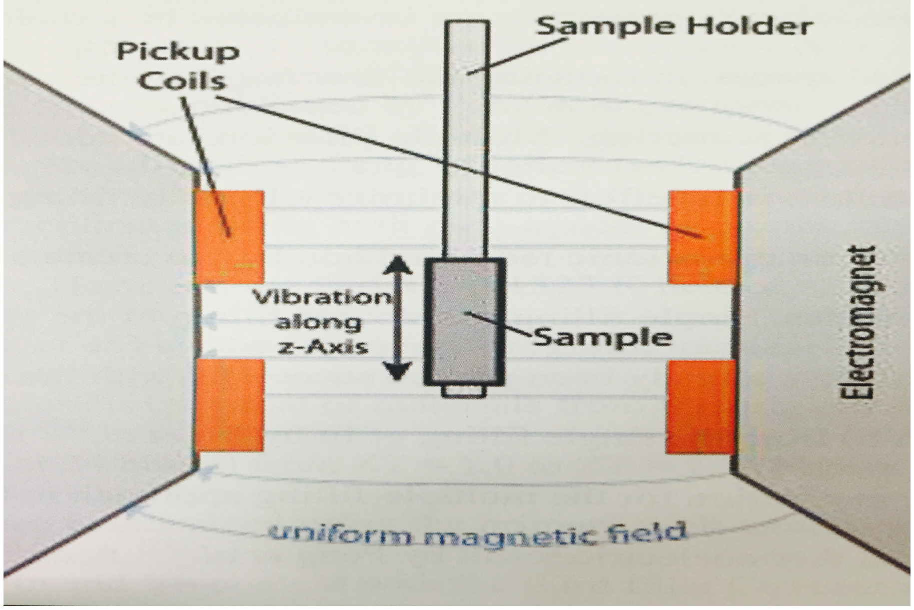

Figure 5.8: Cartoon of the Vibrating Sample Magnetometer showing the position of the sample to the pickup coils which measure the magnetic moment of the sample [6].

5.3 First principle calculations

Density functional theory (DFT) calculations were performed with Vienna ab initio Simulation Package (VASP, version 5.3.3) [62, 63]. The Kohn-Sham equations were solved with the projector-augmented wave (PAW) method [64, 65], using the Perdew-Burke-Ernzerhof (PBE) exchange and correlation functional [66]. Three types of skutterudite structures were studied, including $CoSb_3$, La-filled $CoSb_3$, and La-filled $CoSb_3$ skutterudites with single vacancy or double vacancies. The structure of Co_4Sb_{12} was constructed by expanding the primitive body-centered cubic (bcc) lattice Co_4Sb_{12} into a 2×2×2 bcc supercell $Co_{32}Sb_{96}$, which contains eight dodecahedron voids, each enclosed by eight Co atoms and six pairs of Sb atoms. The structure of La-filled Co_4Sb_{12} was then constructed by filling one of the eight voids in $Co_{32}Sb_{96}$, giving $LaCo_{32}Sb_{96}$ (or equivalently $La_{0.125}Co_4Sb_{12}$) with a filling fraction of 12.5 *at*% that is close to the lower end of experimentally studied filling range of 10-60 *at*%. Finally, the structures of La-filled Co_4Sb_{12} with single vacancy were created by removing one Sb atom at six random positions while those with double vacancies were created by removing two directly bonded Sb pairs at six random positions, giving $LaCo_{32}Sb_{95}$ (or equivalently $La_{0.125}Co_4Sb_{11.875}$) and $LaCo_{32}Sb_{94}$ (or equivalently $La_{0.125}Co_4Sb_{11.75}$), respectively. On the basis of our validation of exchange-correlation functionals against the experimental lattice information of Co_4Sb_{12}, the structures of Co_4Sb_{12} and La-filled Co_4Sb_{12} were first optimized using a nonlocal optB86b-vdW functional entertaining van der Waals (vdW) correction. Both lattice vectors and atomic positions were relaxed until the Hellmann-Feynman forces were smaller than 0.01 eV/$\mathring{A}$. For the La-filled Co_4Sb_{12} with vacancies, only atomic positions were relaxed while the lattice vectors were kept the same as experimental values of Co_4Sb_{12}. All of the optimized structures were then used for static electronic structure calculations with PBE functional. Non-spin-polarized calculations were performed for the system without La filling while spin polarization was turned on for the La-filled systems without and with defects. The Brillouin-zone integrations were performed on a Γ-centered 4×4×4 k-point grid, the kinetic energy cutoff for plane waves was set to 500 eV, the convergence criterion for electronic self-consistency was set to 10-5 eV, and the accurate precision setting was adopted to avoid wrap around errors. Spin-orbit coupling (SOC) effect was tested for the primitive lattice of the parent system Co_4Sb_{12} showing that the SOC effect is weak, in agreement with an earlier expectation. SOC calculations could not be afforded for the La-filled systems without and with defects due to the large size of the supercell. However, SOC calculations for other $LaRu_4X_{12}$ (X=P, As, Sb) skutterudites indicate no pronounced SOC effect in the vicinity of the Fermi level, implying that the SOC effect is negligible for the La-filled systems under study in the present work. Band structures were sampled in the reciprocal space along primitive-based high symmetry k-points Γ (0, 0, 0), H (0.5, -0.5, 0.5), N (0, 0, 0.5), and P (0.25, 0.25, 0.25). Fermi surface was calculated by using Wannier90 program, and then visualized with XCrysDen program.

Chapter 6

Probe the Role of La Fillers and Sb Vacancies in $\mathrm{CoSb_3}$ Skutterudites by Density Functional Theory Calculations and Experimental Studies

As stated in my research goal and strategy chapter, we will use La as a single control to investigate the doping-nanocompositing-filling mechanism on TE properties. Meanwhile, the empty f orbital of La enable us to pry into the physical identity of the guest atom, as well as the interplay between the La filler and Sb vacancies, which helps explore the role of guest atom that cannot be explicitly indicated by experimental results.

6.1 Experimental and data analysis

Five samples with different La filling fraction (y=0.1,0.2,0.3,0.4 and 0.6) were synthesized and their thermal and electrical properties were characterized following the procedures described in chapter 5. According to Shi *et al.* [45], the theoretical FFL for single La filled in $\mathrm{CoSb_3}$ skutterudite is 23 *at*%, so we purposely vary the filling factor so that we have both samples with under and over filling fraction limit fillers. Scanning electron microscopy (SEM) confirms average grain size and electron differential spectroscopy (EDS) mapping was used to confirm the element composition as well as the existence of the secondary phase.

XRD structure and magnetic property analysis for La-Sb secondary phase. We picked out samples with filling factor just below FFL and far above FFL to examine trace of secondary phases. Fig. 6.1 displays the XRD patterns of the $\mathrm{La_yCo_4Sb_{12}}$ (y=0.1,0.2,0.4,0.6) skutterudites, from where the main diffraction peaks match with the standard $\mathrm{Co_4Sb_{12}}$ pattern, no extra peaks from other phases were observed. In enlarged figure attached near 37°, we can see the peak tends to shift to a higher angle as more La is filled in $\mathrm{Co_4Sb_{12}}$ except $\mathrm{La_{0.6}Co_4Sb_{12}}$. Based on Bragg's law $2dsin\theta = \lambda$, in which d is the space between two parallel planes, and λ is the incident wave length which is a constant. We can make a *rough* deduction about the relation of d-spacing of samples with different filling factors:

$d_{\mathrm{La_{0.1}Co_4Sb_{12}}} > d_{\mathrm{La_{0.6}Co_4Sb_{12}}} > d_{\mathrm{La_{0.2}Co_4Sb_{12}}} > d_{\mathrm{La_{0.4}Co_4Sb_{12}}}$. Except for $\mathrm{La_{0.6}Co_4Sb_{12}}$, others follow the larger filling factor with a smaller d-spacing rule. This makes us think that the FFL might be filler-content dependent in La-filled $\mathrm{CoSb_3}$. When above the FFL, filling and formation of secondary phase are competing that results in larger amount of filler ending up with a smaller FFL. The "filler" in the cage still plays as "static point defect" to electron and phonon transportation, but the excess amount

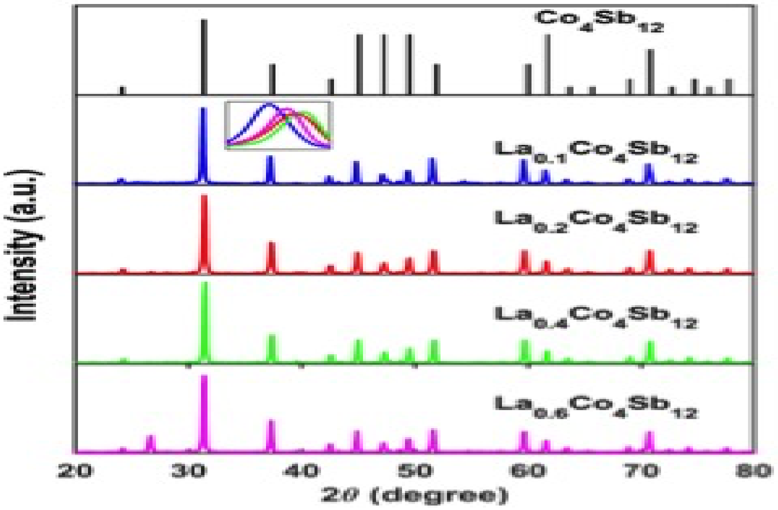

Figure 6.1: X-ray diffraction (XRD) pattern for pristine Co_4Sb_{12} and $La_yCo_4Sb_{12}$ (y=0.1,0.2,0.4,0.6) samples. The enlarged figure is near 37°, which is to showcase the peak shift by La doping.

outside of cage may exist in the form of La-Sb secondary phase. To prove this, we can either look for evidence through microscopy or transport property. The SEM picture of $La_{0.4}Co_4Sb_{12}$ (Fig. 6.4) clearly prove the existence of secondary phase (The dark area), and the EDS analyze the ratio of La to Sb in secondary phase is approximately 2:1, so the form of secondary phase might be La_2Sb.

On the transport property, the carrier concentration may be a good indicator of the existence of the secondary phase. The excess amount of La outside of the cage cannot be stable without bonding with Sb, this will cause the electrons from Co becoming itinerant electrons in the matrix. So the increase of carrier concentration while increasing the filling factor of La above FFL would definitely indicate the existence of secondary phase. However, due to the strong magnetic influence from La atom on Hall measurement, the Hall data cannot be trusted, instead, the susceptibility of $La_{0.4}Co_4Sb_{12}$ and $La_{0.6}Co_4Sb_{12}$ were measured as a function of temperature. Based on Curie-Weiss law $\chi = \chi_0 + \frac{C}{T-\theta}$ (C is the specific material curie constant, and is

Curie temperature while T is the absolute temperature), χ_0 is contributed from the diamagnetic effect and Van Vleck paramagnetism from Co_4Sb_{12} matrix and Pauli paramagnetism from free electrons. Therefore, without tedious calculations, we can roughly deduce that $La_{0.6}Co_4Sb_{12}$ has more carrier concentration than $La_{0.4}Co_4Sb_{12}$ by comparing the y-intercept of the flat part on the plot. Also, based on the literature study, the temperature and grain size independent diamagnetism from Co_4Sb_{12} is about -7.4×10^{-5} to -8.8×10^{-5} emu/mol, which is very close to that of Cobalt ion, and the Van Vleck contribution is even smaller than this. After taking these two out of the total susceptibility, as is shown in Fig. 6.3, we are able to roughly approximate the contribution from the La-Sb secondary phase. In order to figure out the formation of the La-Sb secondary phase, we used Curie-Weiss law to fit Fig. 6.3 that has already taken out the effect from Co_4Sb_{12} matrix or Co ion. All the fitting parameters are listed in Table 6.1. Based on the relation $C = \frac{\mu_B^2}{3k_B N g^2 J(J+1)}$, in which N is the number of magnetic atoms per unit volume, g the *Lande g factor*, μ_B the Bohr magneton, J the angular momentum quantum number, the effective magnetic moment of $La_{0.4}Co_4Sb_{12}$ and $La_{0.6}Co_4Sb_{12}$ is 0.87 and 1.16 respectively. Normalizing into one unit cell, we can get ≈ 2.175 and ≈ 2.0 for La-Sb secondary phase contribution in two samples respectively. La has two oxidation states +3 and +2, the former one is more stable. But according to J.H. Van Vlecks prediction [67], the effective magnetic moment from +3 lanthanum is zero, but our data still shows a relatively steep curve below 20K which is due to paramagnetic contribution. So we can exclude the +3 La ion contribution. But the effective magnetic moment for La^{+2} cannot be found in any literature probably due to its fairly instability. But La element has paramagnetic property when it forms double hexagonal closed-packed crystal structure, we think the paramagnetic contribution may be from the secondary phase La_2Sb whose structure is composed of an alternate stacking of La square nets

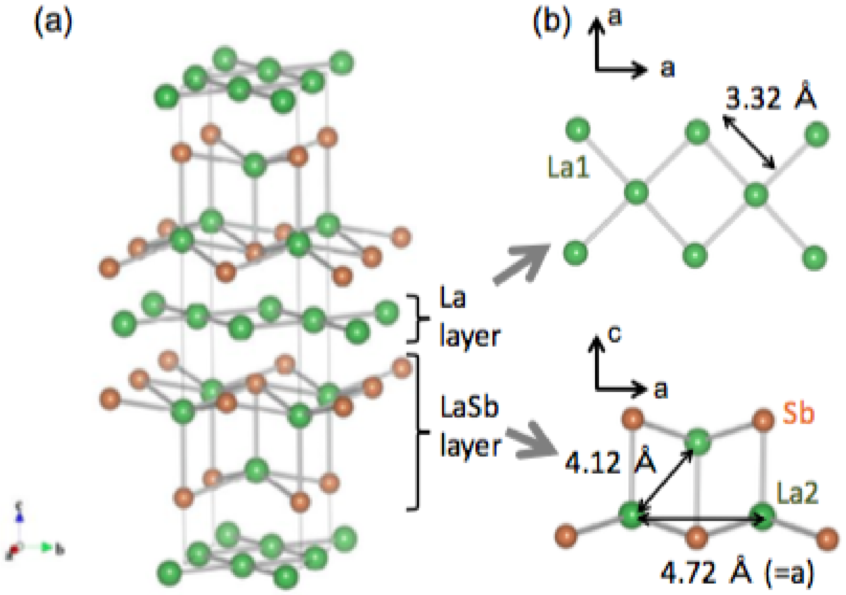

Figure 6.2: (a) Crystal structure of La_2Sb. The structure is composed of the alternate stacking of La square nets and LaSb layers. (b) Local coordination of these layers and the La-La separation [68].

Table 6.1: Equation $\chi = A + \frac{C}{T-B}$ was used to fit the susceptibility data.

	A	B	C
$La_{0.4}Co_4Sb_{12}$	2.07×10^{-6}	-29.30072	0.09358
$La_{0.6}Co_4Sb_{12}$	0.00129	-107.92649	0.16606

and LaSb layers [68](Fig. 6.2). The LaSb layers are quite stable with La^{+3} and showing now magnetism, so the La square nets may have something to do with the paramagnetism. And this prediction matches pretty well with the EDS result. But further investigation have to be made on this issue.

Thermoelectric properties. The seebeck coefficient (Fig. 6.5) changes sign when La is filled to and above 10 *at*%, which suggests the pristine Co_4Sb_{12} is a *p* type semiconductor with the Fermi level lie in the valence band. When 10 *at*% at of La was filled in the void, the electrons from La compensate the concentration of holes and pull up the Fermi level in valence band. Until the valence electrons from filler La

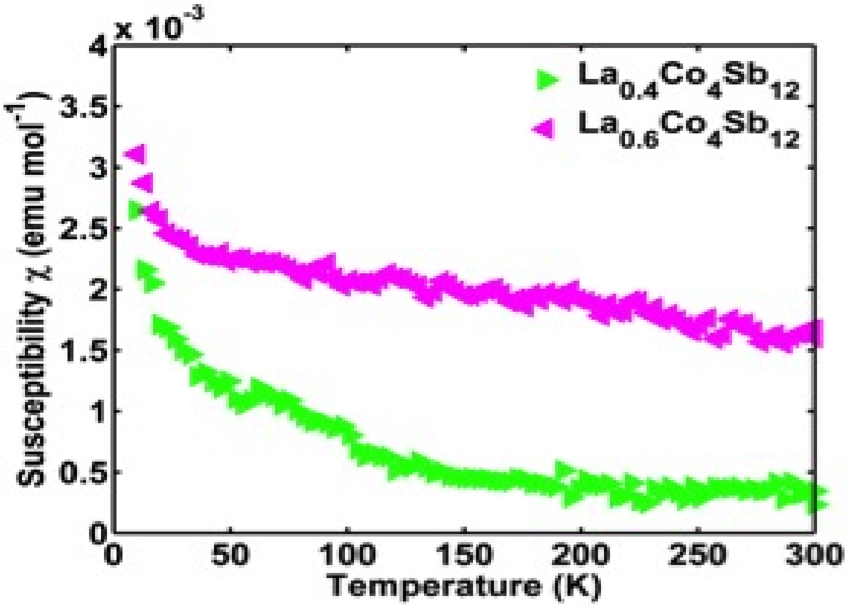

Figure 6.3: Susceptibility for $La_yCo_4Sb_{12}$ (y=0.1, 0.4, 0.6) skutterudites

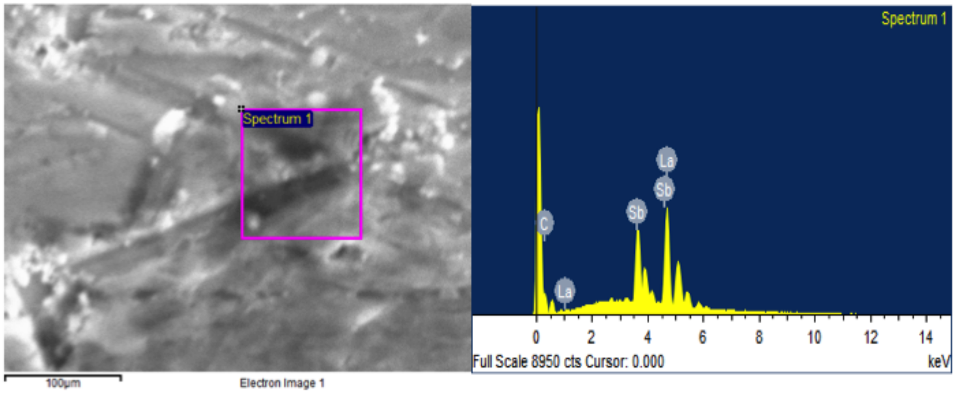

Element	Weight%	Atomic%
Sb L	41.22	20.01
La	78.39	33.35

Figure 6.4: The SEM photo of $La_{0.4}Co_4Sb_{12}$, the dark area is the secondary phase with $La : Sb \approx 2 : 1$

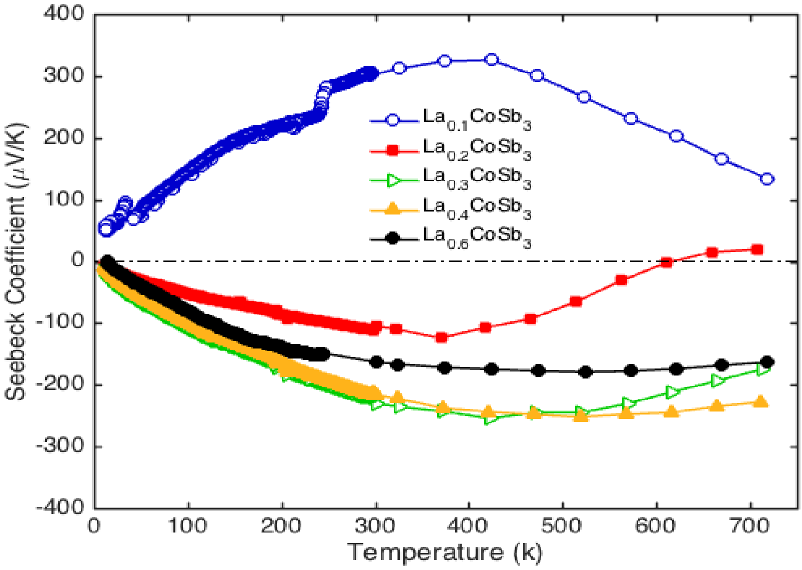

Figure 6.5: Temperature dependent seebeck coefficient for $\mathrm{La_yCo_4Sb_{12}}$ (y=0.1,0.2,0.3,0.4,0.6), the sign turns over for $rmLa_{0.2}Co_4Sb_{12}$ at high temperature.

atom totally compensate the holes, a little extra electrons contribution would change the system into *n* type semiconductor and push the Fermi level up into conduction band. The Seebeck sign change of $\mathrm{La_{0.2}Co_4Sb_{12}}$ when temperature increases may be due to the narrow band gap and the position of the Fermi level. Except $\mathrm{La_{0.1}Co_4Sb_{12}}$, the peaks of seebeck coefficient for other samples tend to shift to a higher temperature as filling factor of La increased, this suggests the band gap changes significantly with filling. This shift can also move the ZT peak to a higher temperature range that makes it possible to change the working temperature of the materials (As in Fig. 6.8). The magnitude of Seebeck coefficient also imply that the carrier concentration of $\mathrm{La_{0.6}Co_4Sb_{12}}$ is the highest which matches with our susceptibility result.

From Fig. 6.6 we can also see that the electrical conductivity for $\mathrm{La_{0.1}Co_4Sb_{12}}$ shows a semiconductor behavior, as the addition of La, the electrical conductivity tend

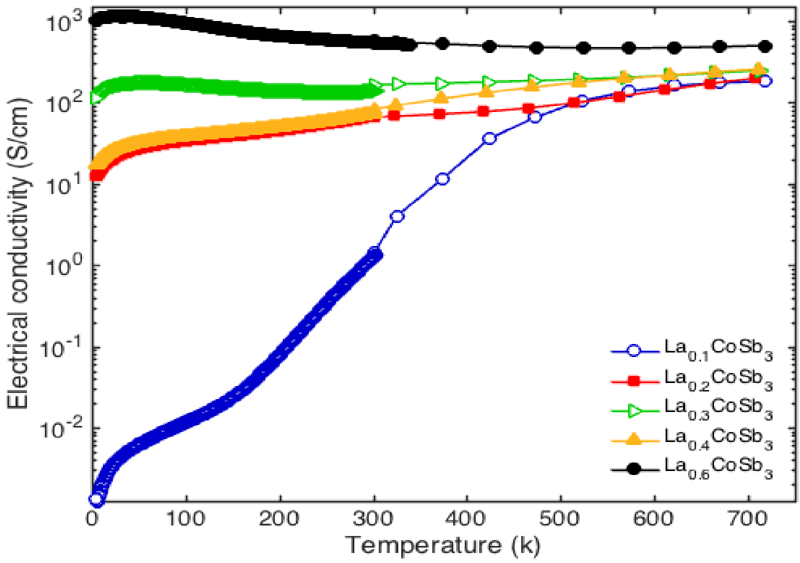

Figure 6.6: Temperature dependent electrical conductivity for $La_yCo_4Sb_{12}$ (y=0.1,0.2,0.3,0.4,0.6). The huge increase of electrical conductivity for $rmLa_{0.6}Co_4Sb_{12}$ is from deficiency doping.

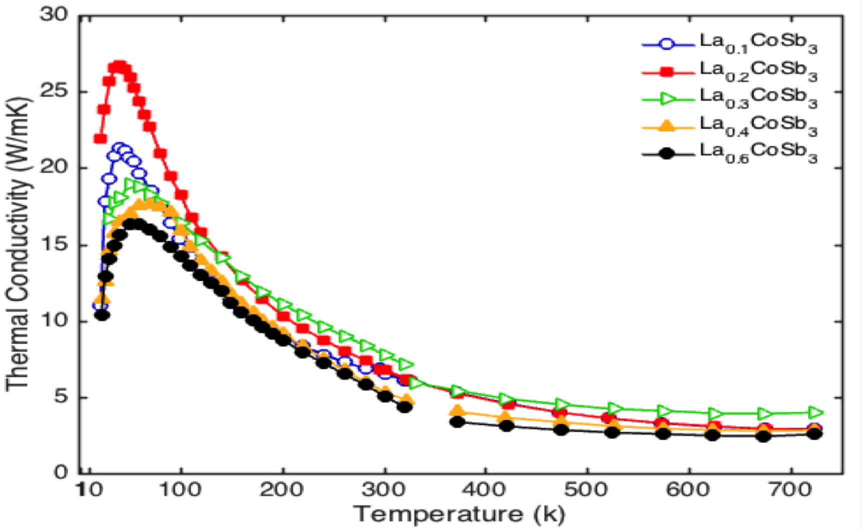

Sample name	$La_{0.1}Co_4Sb_{12}$	$La_{0.2}Co_4Sb_{12}$	$La_{0.3}Co_4Sb_{12}$	$La_{0.4}Co_4Sb_{12}$	$La_{0.6}Co_4Sb_{12}$
Power of T (a)	0.9756	0.3305	0.2443	0.3185	0.4168

Figure 6.7: Temperature dependent thermal conductivity for $La_yCo_4Sb_{12}$ (y=0.1,0.2,0.3,0.4,0.6). They don't differ that much at high temperature. The table below is to show the T^a dependence of κ_l at low temperature (T<60K)

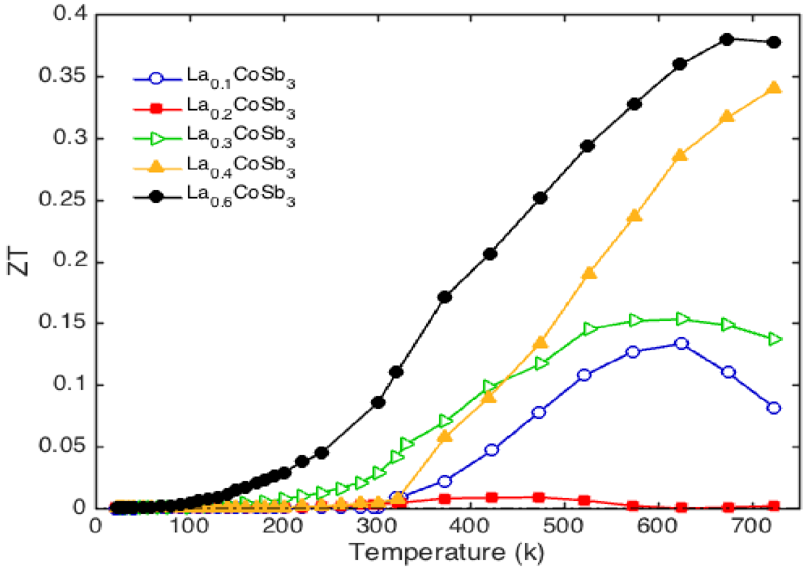

Figure 6.8: Figure of Merit of $La_yCo_4Sb_{12}$ (y=0.1,0.2,0.3,0.4,0.6)

to have a metallic behavior. The electrical conductivity for $La_{0.6}Co_4Sb_{12}$ is several magnitude larger than others, especially compared with $La_{0.4}Co_4Sb_{12}$. This can be explained by the Sb deficiency doping, which validates the existence of La-Sb secondary phase that cause a large increment of carrier concentration. Fig. 6.7 shows the temperature dependence of the lattice thermal conductivity of $La_yCo_4Sb_{12}$ samples. While the pristine sample has a very high thermal conductivity of 8.8 W/mK, the filling of La can effectively reduce it down to below 3 W/mK for $La_{0.6}Co_4Sb_{12}$ at temperature from 600 K to 700 K. Theoretically speaking, static point defects would scatter phonons and lower thermal conductivity more effectively at high temperature, and also when they are at their most disordered states, say, when the cage of skutterudite is filled to 50%. However, the FFL of La is only around 20 *at*%. But when look at the lattice thermal conductivity for all $La_yCo_4Sb_{12}$ (y=0.1,0.2,0.3,0.4,0.6), it decreases continuously with the increase of y, and this effect is especially manifested at low-temperature (T< 150K). As the La concentration increases, the suppression of

κ_l seems to saturate. The slope of lines at low-temperature (T< 60K) are calculated to illustrate the T^a dependence of κ_l at low temperature [69], where a=0.9756, 0.3305, 0.2443, 0.3185 and 0.4168, respectively. The observation that $\kappa_l \propto T^1$ for T<30K for all samples is a strong indication of the presence of electron-phonon interaction. The SEM shows that the size of the La-containing secondary phase is 300-500 nm. Base on the equation $\lambda = \theta/T$ a in which λ is phonon wavelength and θ is the Debye temperature, T is 300K and a is grain constant, we can roughly know the phonon wavelength is at the same scale as grain constant that is $\approx 1nm$. So the secondary phase is too large to scatter phonons. But the secondary phase can cause the Sb deficiencies that indirectly bring more point defects into the system, which we believed is the reason for the slightly decrease in lattice thermal conductivity with an increase in y. Due to decent PF and a fairly low thermal conductivity, $La_{0.6}Co_4Sb_{12}$ has a ZT close to 0.4 around 700K as in Fig. 6.8. Not very surprisingly, the increase in ZT for $La_{0.6}Co_4Sb_{12}$ is largely due to the improve in electron transport properties.

So far, the experimental results only indicated the existence of La-Sb secondary phase and an observable monotonously increasing σ with La addition. Although the slightly decrease in κ_{ph} with La addition can imply that La dose not have a strong influence on phonon scattering, the evidence is not obvious enough to indicate the physical identity of the guest atom La, and how it interact with Sb deficiencies to affect the TE property especially the σ. Therefore, theoretical calculations are necessary.

6.2 Theoretical calculation result

The first principle calculation and the validation of $CoSb_3$ skutterudite calculation have been discussed in chapter 4 and 5 respectively. Having assured the calculation for the parent structure is right, we will start with the calculation result of La filled Co_4Sb_{12} so as to figure out the role of La.

Exploring the band structure of $La_{0.125}Co_4Sb_{12}$. The spin-polarized electronic band structure and DOS of $LaCo_{32}Sb_{96}$ are shown in Fig. 6.9(b). Spin-polarized calculations for $CoSb_3$ skutterudite have been reported for its surface properties [70], but are rarely applied to investigate the role of filler atoms. As can be seen from Fig. 6.9(b), the spin-polarized band structure of La-filled skutterudite bears a large degree of similarity to the bands of its parent structure as shown in Fig. 6.9(a). This indicates that the bands of $Co_{32}Sb_{96}$ are rigid and the low La filling fraction appears to simply raise the Fermi level to a position slightly above the valley at the N point. On the other hand, the spin-polarized results reveal a notable feature that the two spin channels display a large band offset for the conduction bands. For instance, the CBM at the Γ point for the spin-down channel is raised up with respect to that for the spin-up channel while the VBMs for both spins are essentially the same. As a result, the direct band gap is larger for the spin-down channel than the spin-up counterpart. In addition, the Fermi Energy is located at ca. 0.14 eV above the CBM of the spin-up channel and at cal. 0.09 eV above the CBM of the spin-down channel. This spin-polarization effect can be also seen from the DOS curves. The DOS at the Fermi level for the spin-up channel is enhanced to nearly the high DOS peak at the expense of that for the spin-down channel which is significantly reduced. Also based on the partial DOS analysis (Fig. 6.10(b)), it can be seen that the two spins are nearly degenerate for valence states but show a large DOS offset for the conduction states. Again, the DOS at the Fermi level is significant only for the spin-up channel and it consists of a hybridization of Cos d, Sbs *s* and *p*, and the filler Las *d* states. The filler Las *s* state shows negligible contribution to the DOS at the Fermi level and therefore all of the three electrons in Las valence shells according to its electronic configuration [Xe]$5d^1 6s^2$ appear to participate in the hybridization in the form of *d* states. In addition to the electronic properties, the spin-polarized calculations also gave a magnetization of 2.35 μB for $LaCo_{32}Sb_{96}$, in line with the large band offset between the two spin channels. In terms of energetics, the spin-polarized solution is 2 meV more stable than the non-spin-polarized solution, indicating that the ground state of $LaCo_{32}Sb_{96}$ is the former. However, the energy difference is very small and therefore there may not be a preference for long-range spin ordering. These small energy differences indicate that the long-range spin ordering is not favored for $LaCo_{32}Sb_{96}$, in agreement with our experimentally observed paramagnetic instead of ferromagnetic properties. And also this strong spin polarization show the potential for La filled $CoSb_3$ skutterudite to be good candidate for spintronics material that concerns spin-dependent electron transport phenomena in solid-state devices.

Sb *5p* and La *5d* orbital hybridization and its effects. The total density of states (DOS) and partial DOS of La-filled $La_{0.125}Co_4Sb_{12}$ indicate that both states near CBM and VBM mainly originated from Co *3d* electrons and Sb *5p* electrons (Fig. 6.10). Compared with the pristine Co_4Sb_{12} DOS, the ones with La-filling have some changes near CBM and VBM. Specifically, the ratio of DOS_{Sb5p}/DOS_{Co3d} is decreased from 2.46 for Co_4Sb_{12} to 1.56 for $La_{0.125}Co_4Sb_{12}$ near VBM and increased from 0.14 for Co_4Sb_{12} to 0.18 for $La_{0.125}Co_4Sb_{12}$ near CBM. This evolution indicates that the energy of Co *3d* electrons and Sb *5p* electrons become closer [33], and the *p*-*d* hybridization between Co and Sb has thus been enhanced in $La_{0.125}Co_4Sb_{12}$ [33]. To explain this enhancement of *p*-*d* hybridization between Co and Sb in La-filled $CoSb_3$ system, we

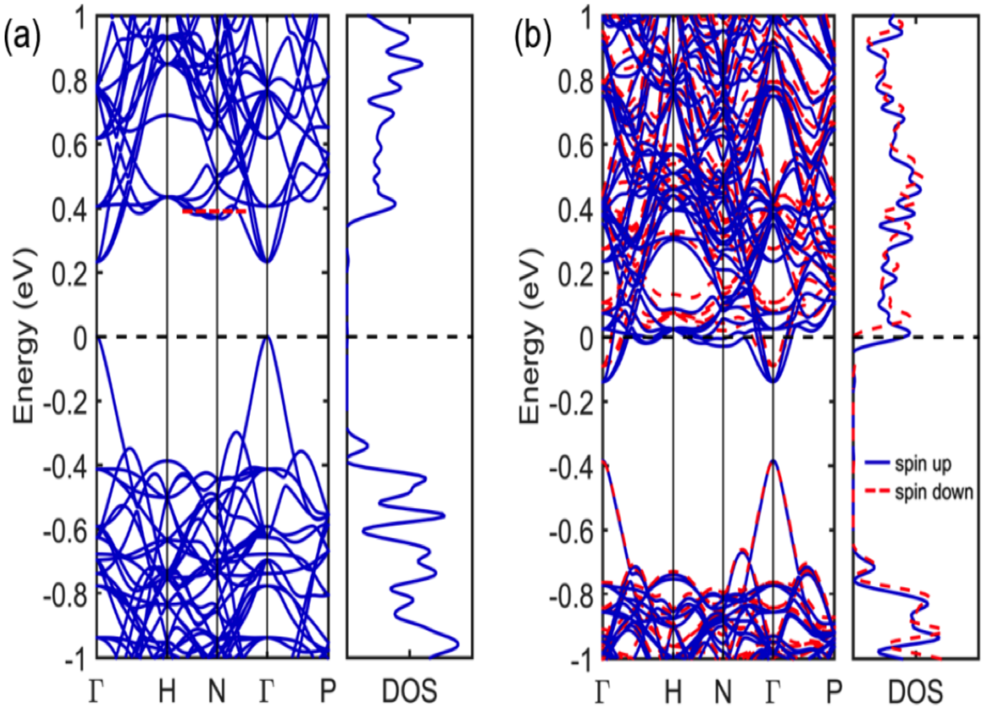

Figure 6.9: Band structure and total density of states of pristine Co_4Sb_{12} (a) and $La_{0.125}Co_4Sb_{12}$ (b).

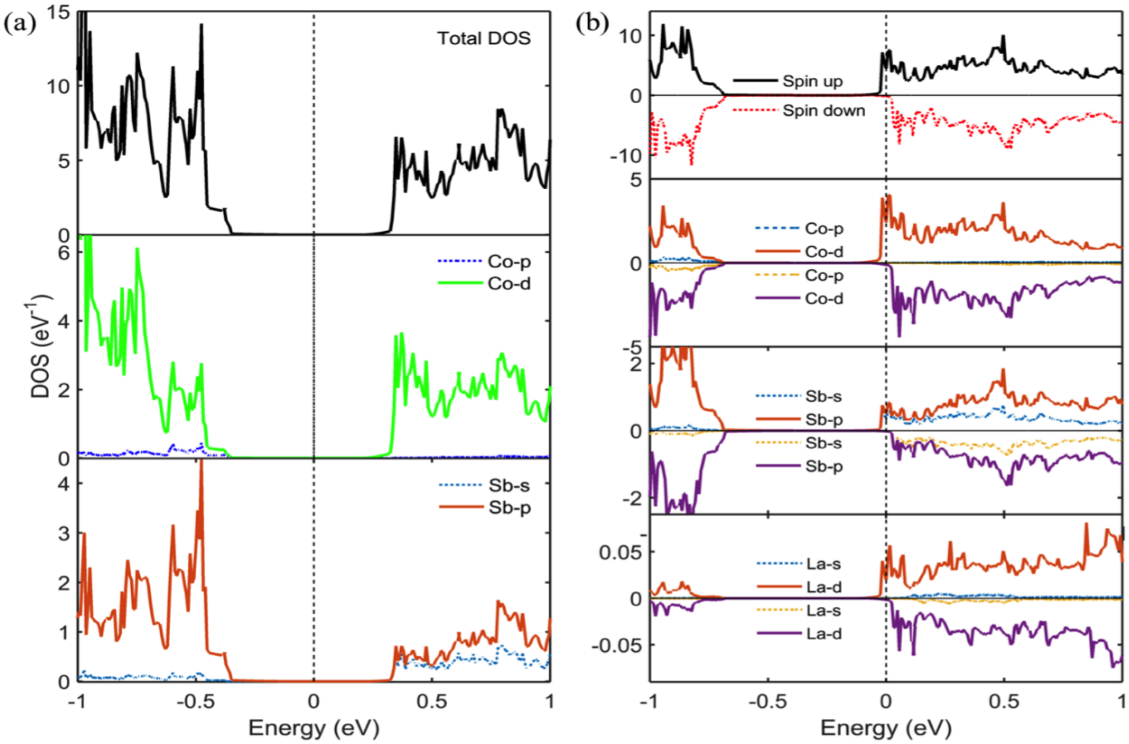

Figure 6.10: Projected density of states (DOS) for Co_4Sb_{12} (a) and $La_{0.125}Co_4Sb_{12}$ with spin polarization (b).

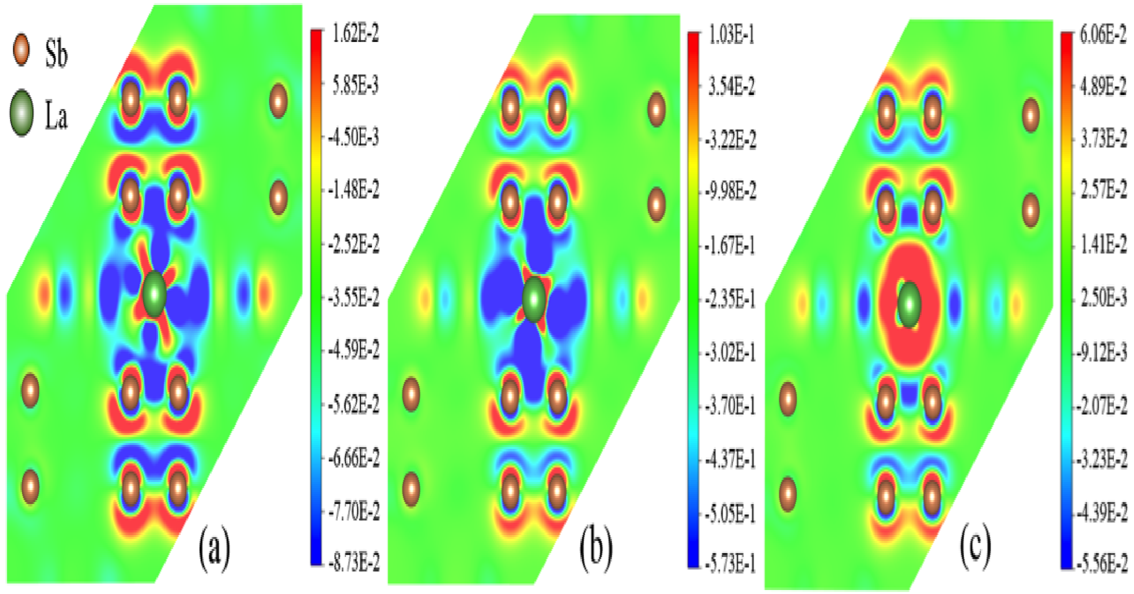

Figure 6.11: Differential charge density (DCD) of $La_{0.125}Co_4Sb_{12}$ projected on $(1\bar{1}1)$ plane. A primitive $2\times2\times2$ supercell is filled by one La atom at the central cage to give the filling factor of 12.5%. The DCD is presented based on the total charge density (a), and is broken down to a spin-up component (b) and a spin-down component (c) based on the corresponding spin-up and spin-down charge densities. The unit of charge density is $eV/\mathring{A}^3$.

analyzed the partial DOS of $La_{0.125}Co_4Sb_{12}$ in the range of $-10eV \sim 6eV$. As in Fig. 6.12. Although part of *6s* states are distributed far below -1eV that are deeply bounded in valence band, there are still some part of *6s* states distributed close to and slightly above Fermi level, which indicates only part of *6s* states would contribute to electrical conduction.

For *5d* electrons, although a very small amount of *5d* states are distributed close to -1eV that are deeply bounded in valence band, most of the *5d* states are distributed close to and above Fermi level, which suggests that the almost all La *5d* electrons are contributing to electrical property in La filled $CoSb_3$ system. Which basically means that we now have one almost empty *s* orbital($6s_0$) and five empty *5d* orbitals ($5d_0$) available. But considering the *6s* orbitals is far in distance compared to orbitals with

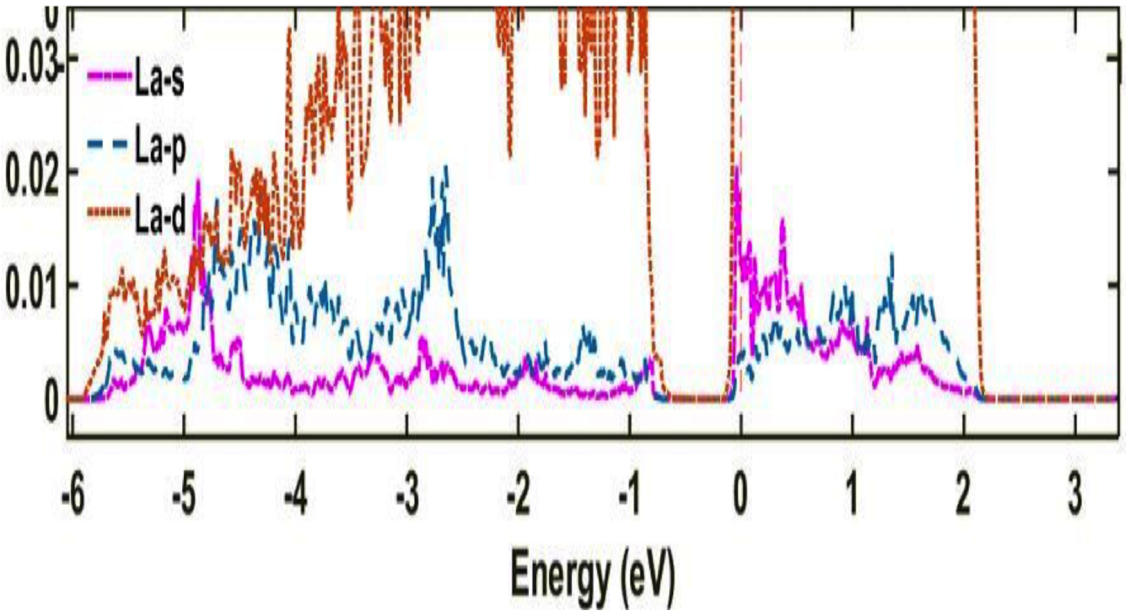

Figure 6.12: Partial density of state of $La_{0.125}Co_4Sb_{12}$ in the range of $-10eV \sim 6eV$

main quantum number 5, *6*s_0 orbital is out of option for interaction. Therefore, La may provide five empty $5d_0$ orbitals for the *p*-*d* hybridization between La and Sb. This can be shown in figure of differential charge density plot (Fig. 6.11). The red color represents the electron rich area and the light green color represents electron depletion area. These two spots clearly show the evidence of charge transfer between La and Sb that also indirectly prove the hybridization of *p*-*d* oribitals between La and Sb. Therefore, we can say that **the enhancement of *p*-*d* orbital hybridization between Co and Sb must stem from the *p*-*d* orbital hybridization between La and Sb**. The importance of *p*-*d* orbital hybridization between La and Sb thus can be concluded as follows: 1) According to Zhao *et al.*, it can cause a charge transfer from La to Sb and produce two types of atomic-scale electric fields near the La-filled Sb_{12} icosahedron. Since the framework of Sb_{12} icosahedron acts as the passage of majority carriers in La-filled $CoSb_3$, the atomic-scale electric fields with positive charge at the framework in La-filled Sb_{12} icosahedron may enhance mobility [33]. This is thermoelectrically favorable. 2) The charge transfer can also prove the role of La as a filler in $CoSb_3$, not a rattler that is supposed to loosely bound with surrounding atoms. This agrees with the small decrease of κ_{ph} with La addition even when La amount is below FFL. In this case, La became part of the host matrix and did not scatter phonons as greatly as a rattler do.

Multiple band conduction in $La_{0.125}Co_4Sb_{12}$. As described above, La filling raises the Fermi level to a position slightly above the valleys at the N point (Fig. 6.9(a),(b)), which correspond to the valley in the middle of Γ-N zone for the primitive bcc cell (Fig. 6.13). Snyder and coworkers recently pointed out that raising the Fermi level to the valley of Co_4Sb_{12} leads to twelve isolated Fermi pockets which explain the term degenerate valleys. They used these "degenerate valleys" to explain the high electrical conductivity in $Yb_{0.25}Co_4Sb_{12}$ and call it multiple band conduction. Due to the high effective mass, the charge carriers in the degenerate valleys at the Fermi level play a crucial rule for the extraordinary thermoelectric performance at high filling. The Fermi surface for $Co_{32}Sb_{96}$ in Fig. 6.14(a) at 0.143 eV above the CBM as indicated by the red dashed line in Fig. 6.9(a) shows a core pocket in the center of the Brillouin zone and twelve degenerate half pockets surrounding the core. The core pocket in Fig. 6.14(a) consists of three layers of iso-energy surface corresponding to the three lowest conduction bands (the inner two layers are invisible). When 12.5 at% La is filled in the parent skutterudite giving $La_{0.125}Co_4Sb_{12}$, the number of extra electrons is 0.375 per unit cell. Compared to the 0.5 electrons per unit cell for $Yb_{0.25}Co_4Sb_{12}$, this amount of extra electrons is barely enough to lift the Fermi level above the valley bottom. However, due to the presence of spin-polarization, the Fermi level for the spin-up channel is indeed located in the degenerate valleys while that for the spin-down counterpart is below the degenerate valleys (Fig. 6.9(b)). Consequently,

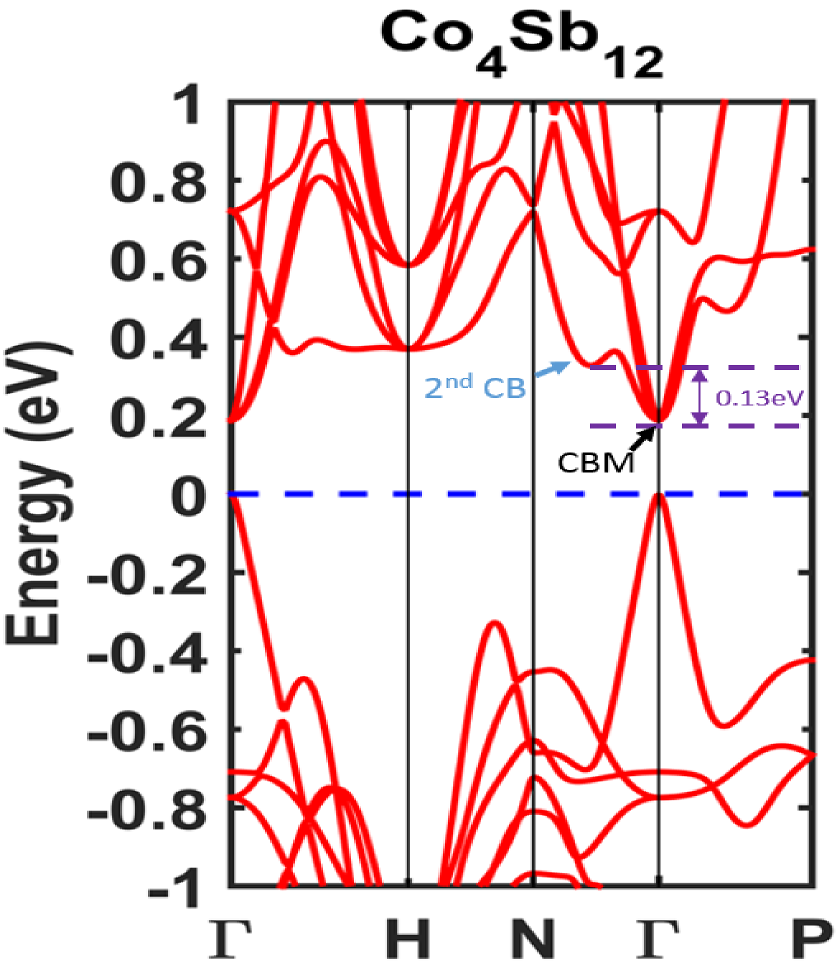

Figure 6.13: WANNIER90 calculation of band structure of $CoSb_3$ in 1×1×1 primitive cell.

the Fermi surfaces for the two spin channels show a large difference. As can be seen in Fig. 6.14(b), the Fermi surface for the spin-down channel only shows a core pocket while that for the spin-up channel shows large peripheral open pockets joined together. There are two layers of peripheral pockets (the inner layer being in red) since the Fermi level is slightly above the second valley band at the N point. This indicates an asymmetric contributions of two spin channels to the electronic properties, which may have profound implications for thermoelectrics.

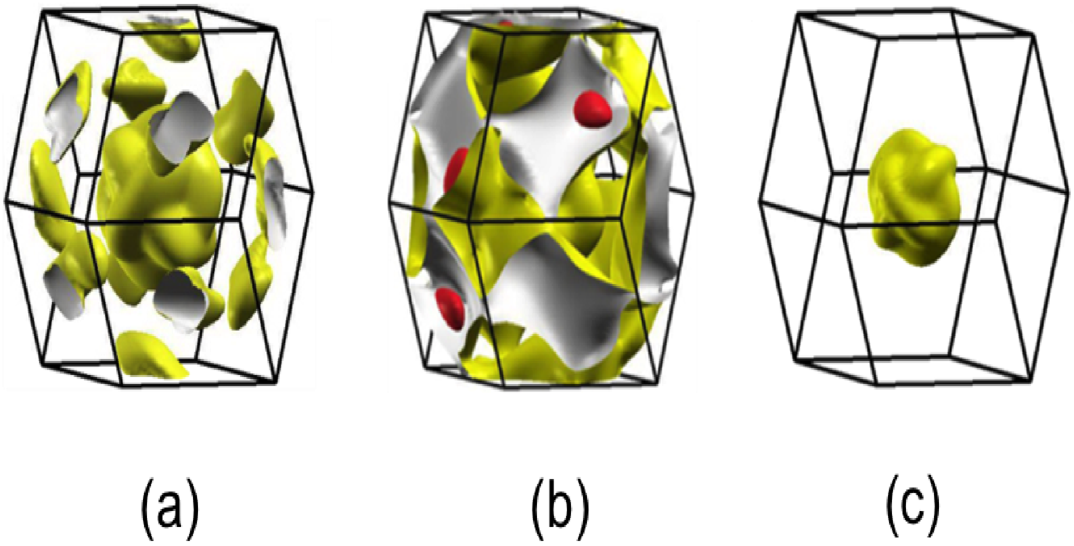

Figure 6.14: (a) Fermi surface for $Co_{32}Sb_{96}$ without spin polarization. (b) Fermi surface for $LaCo_{32}Sb_{96}$ with spin polarization. The Fermi surface of $Co_{32}Sb_{96}$ is calculated at 0.143 eV above the conduction band minimum (CBM). The Fermi surface of $LaCo_{32}Sb_{96}$ is shown for the spin-up electron and the spin-down electron, respectively.

6.3 Summary

La filled $CoSb_3$ skutterudites have been prepared with the La filling factor varies from below to above FFL for the purpose of revealing the role of La in the $CoSb_3$ skutterudite system and observing enhancement of thermoelectric properties due to over the FFL for single filled skutterudites. The experiment as well as the theoretical DFT calculation indicate the multi-role of La: 1) first as a filler and static point defect scattering phonons. 2) then as La-Sb secondary phase, directly cause Sb deficiencies that also scatter phonons as point defects. $La_{0.6}Co_4Sb_{12}$ achieve a ZT of 0.4 around 700 K which is much better than other $La_yCo_4Sb_{12}$ samples with y=0.1, 0.2, 0.3, 0.4 respectively.The improvement of ZT for $La_{0.6}Co_4Sb_{12}$ is mainly contributed from a slightly decrease of the lattice thermal conductivity and a huge increase of electrical conductivity. Over the FFL reduce the thermal conductivity much less than expected due to the filler nature of La. The huge increase of electrical conductivity is due to the Sb deficiency doping. The band structure of $La_{0.125}Co_4Sb_{12}$ also indicate a strong polarization in the system indicating La filled $CoSb_3$ may have the potential to be spintronic material. Although the ZT for La filled $CoSb_3$ skutterudites is not high enough to compete with other multi-filled skutterudite, this allows us the look more into the physics. Filling over the FFL, not only can help reduce the thermal conductivity, but also increase the hybridization between *d-p* orbitals which may shed more light on band engineering in order to improve thermoelectric performance on more single filled skutterudites.

The band structure calculated in this project only concerned about a perfect Co_4Sb_{12} host material which doesn't match well with experimental result with La addition. The reason for this is due to the Sb loss during sample preparation in experiment. Therefore, a band calculation with certain amount of Sb deficiencies is highly desired, especially for the explanation of the miscellaneous p to n type change with La addition and revealing defects chemistry in the system. This will be discussed in next chapter.

Chapter 7

Further investigation the role of La Fillers and Sb Vacancies in $\mathrm{CoSb}_{3-\delta}$ Skutterudites by Density Functional Theory Calculations.

7.1 Project Motivation

In chapter 6, the calculations on perfect $CoSb_3$ skutterudites with La additions were presented, which showed some discrepancies with the experimental results. The smooth transition from *p* type to *n* type of $La_yCo_4Sb_{12}$ (y=0.1, 0.2, 0.3, 0.4, 0.6) as La content was increased did not match well with the band structure. This discrepancy might originated from the fact that in the sample preparation process, a small amount of Sb would vaporize due to its small vapor pressure, however, when DFT calculations were conducted on this system, only a perfect Co_4Sb_{12} matrix was considered without any loss of Sb. In order to clarify the role of La fillers and Sb deficiencies more precisely, we carried out calculations that allowed us to investigate two cases: *i)* A comparison of the effect of addition of La on $CoSb_{3-\delta}$ skutterudites without differentiating the contribution from spin-up and spin-down electrons. *ii)* A comparison of the effect of amount of Sb deficiencies on $La_{0.125}Co_4Sb_{12-\delta}$ with differentiating the contribution from spin-up and spin-down electrons. The calculations were still on a $2\times2\times2$ primitive cell. In the first case, only the condition with one Sb atom loss was considered, so δ is 0.125. In the second case, for calculation simplicity, only two types of Sb deficiencies were considered: one is only one Sb atom is lost out of eight atoms, so δ is 0.125($La_{0.125}Co_4Sb_{11.875}$), the other situation is two Sb atoms were lost out of eight atoms. so δ is 0.25($La_{0.125}Co_4Sb_{11.75}$).

7.2 Comparison of band structure of $La_yCo_4Sb_{11.875}$ (y=0, 0.125, 0.25) with experimental results.

Band structure of pristine $Co_4Sb_{11.875}$. Either from preparation procedure or over the FFL, Sb deficiency always constructively contribute to electrical conductivity which has already been verified in chapter 5 experimental section. As we may think that with some La filler in the cage that also would donate electrons to the system, the material would be *n* type semiconductor consistently. However, this is not the case from experiment result. The seebeck coefficient indicate a *p* type behavior for both Co_4Sb_{12} and $La_{0.1}Co_4Sb_{12}$. As a thumb of rule, when we mention *p* or *n* type material, it is always from band concept, so it is quite necessary to take a look at the band structure. We start with the pristine $Co_4Sb_{11.875}$ with intentionally taking one Sb atom out of the system. Fig. 7.1 shows the band structure and the density of states. The interesting part here are the three very dispersive impurity bands (two hole like, one electron like) which are never seen for impurity bands in any skutterudite materials before. From the density of states (DOS), we can see that these dispersive bands are mainly from Sb 5*p* electrons.

Usually, the impurity band would be very flat and heavy with zero group velocity. But those three bands are very dispersive indicating they are very **conductive**! For $Co_4Sb_{11.875}$, although the Fermi level is within k_BT range from one hole-like band, the part it is close to has almost zero group velocity and large effective mass, so this dispersion would not contribute to electrical property, which explains the very low electrical conductivity of $Co_4Sb_{11.875}$ compared to other filled $Co_4Sb_{11.875}$. One more important result from this band structure is that it perfectly explained the *p* type of the pristine $Co_4Sb_{11.875}$ we usually get from measuring the Seebeck coefficient of the sample. And this can be seen from the proximity of the Fermi level to two hole-like bands.

Band structures of $La_yCo_4Sb_{11.875}$ **(y=0, 0.125, 0.25)**. Fig. 7.2 shows the band structure of $Co_4Sb_{11.875}$, $La_{0.125}Co_4Sb_{11.875}$ and $La_{0.25}Co_4Sb_{11.875}$ respectively. With one La atom filled into the cage, the Fermi level has been shifted up into the three impurity bands in the band gap, since it is still close to two hole-like bands and stay in one k_BT range to conduction band minimum (CBM), this still indicates a *p* type behavior which match perfectly with the sign of the Seebeck coefficient for $La_{0.1}Co_4Sb_{12-\delta}$ sample. Also, the addition of one La atom makes that one flat impurity band in Fig. 7.1(a) more dispersive, as is shown in Fig. 7.1(b). And since this single impurity band almost touches the Fermi level in Fig. 7.1(b), indicating it directly contributes to the electrical conductivity in $La_{0.125}Co_4Sb_{11.875}$. As one more La atom is filled into the cage (y=0.25 is on the FFL for La filled Co_4Sb_{12}), Fermi level continuously shift up, touching the CBM edge, while disturbing the distribution of three impurity bands.

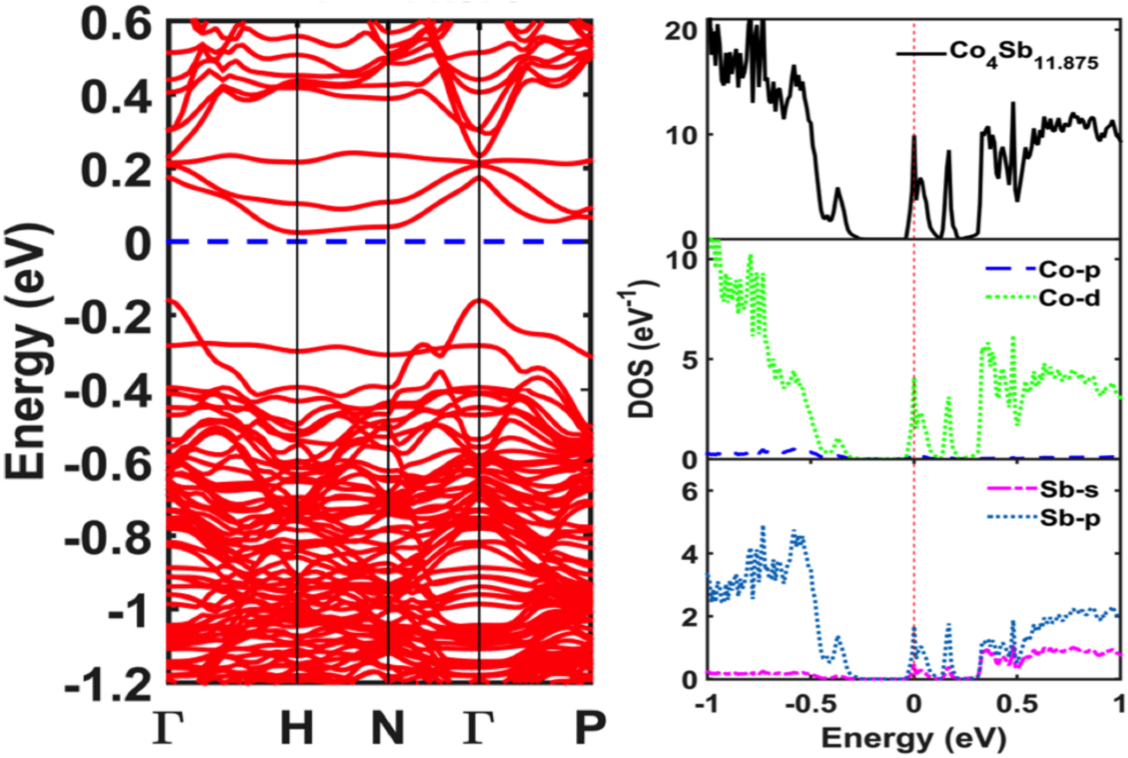

Figure 7.1: The band structure (left) and density of states (right) of $Co_4Sb_{11.875}$. Three dispersive impurity bands can be seen located in the band gap with Fermi level close by.

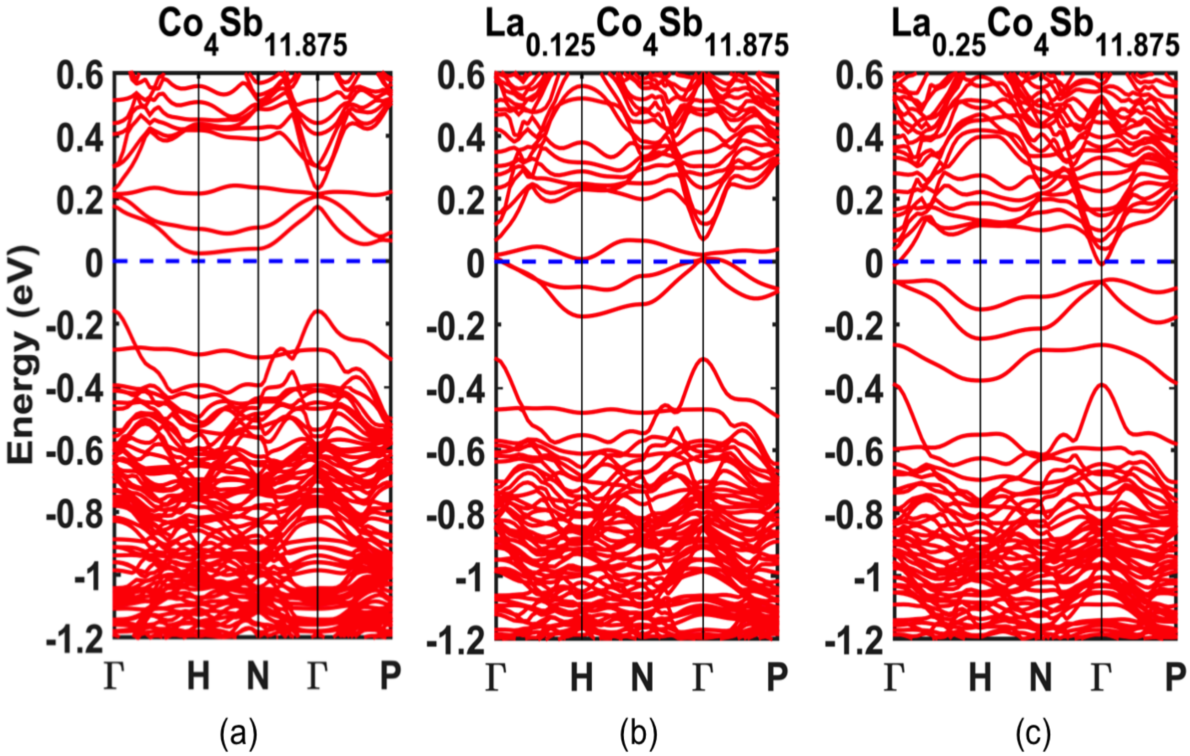

Figure 7.2: The band structure of (a) $Co_4Sb_{11.875}$,(b) $La_{0.125}Co_4Sb_{11.875}$ and (c) $La_{0.25}Co_4Sb_{11.875}$.

This shifting of Fermi level and dispersive impurity bands can be perfectly regarded as one example of the interaction between La fillers and Sb deficiencies. While the amount of La filler control the position of Fermi level, and the Sb deficiencies create the three dispersive impurity bands. From Fig. 7.1(a)-(c), the shifting of the Fermi level also affects how dispersive these three impurity bands are and their individual position. Therefore, we can say that the La filler is very interactive with surrounding Sb atoms/deficiencies which again prove the "filler" identity of La instead of "rattler".

7.3 Comparison of band structures of $\mathrm{La_{0.125}Co_4Sb_{11.875}}$ and $\mathrm{La_{0.125}Co_4Sb_{11.75}}$

The comparison made in section 6.1 indicated the addition of La can shift the Fermi level so that it can interact with three dispersive impurity bands caused by one Sb atom loss. In this section, the amount of La filler is fixed while the amount of Sb deficiencies change. For simplicity, only two cases with one Sb atom loss and two Sb atoms loss will be considered. Fig. 7.3 shows the band structure of $\mathrm{La_{0.125}Co_4Sb_{11.875}}$, the position of the Sb vacancy was randomly chosen, for comprehensiveness, six different spots were chosen. From the six plots we can see that although the vacancy positions were different, they all contributed to the three dispersive impurity bands in the band gap in spite of the shape of these three impurity bands change according to the Sb vacancy position. The blue bands are from spin-up electrons and the red bands are from spin-down electrons. Although Fermi level is close to some dispersive red bands, the parts it is close to have huge effective mass and zero group velocity. Therefore, the contribution to the electrical property from the red bands can be neglected. This is to say that **in $\mathrm{La_{0.125}Co_4Sb_{11.875}}$, only spin-up electrons that are close to Fermi level are constructively contributing to electrical property**. The reason for this is still unknown, but this property can make La filled $\mathrm{Co_4Sb_{12}}$ applicable in spintronics solid-state devices. From Fig. 7.4 we know that the three dispersive impurity bands are mainly from the contributions of Sb atoms nearby the vacant Sb position.

As Sb deficiencies were increased, more dispersive bands would occur in the band gap, as is shown in Fig. 7.5. The variation of these changes from Fig. 7.3 to Fig. 7.5 were hard to trace, and it is hard to weigh the contributions to electrical properties from red (spin-down) and blue (spin-up) bands.

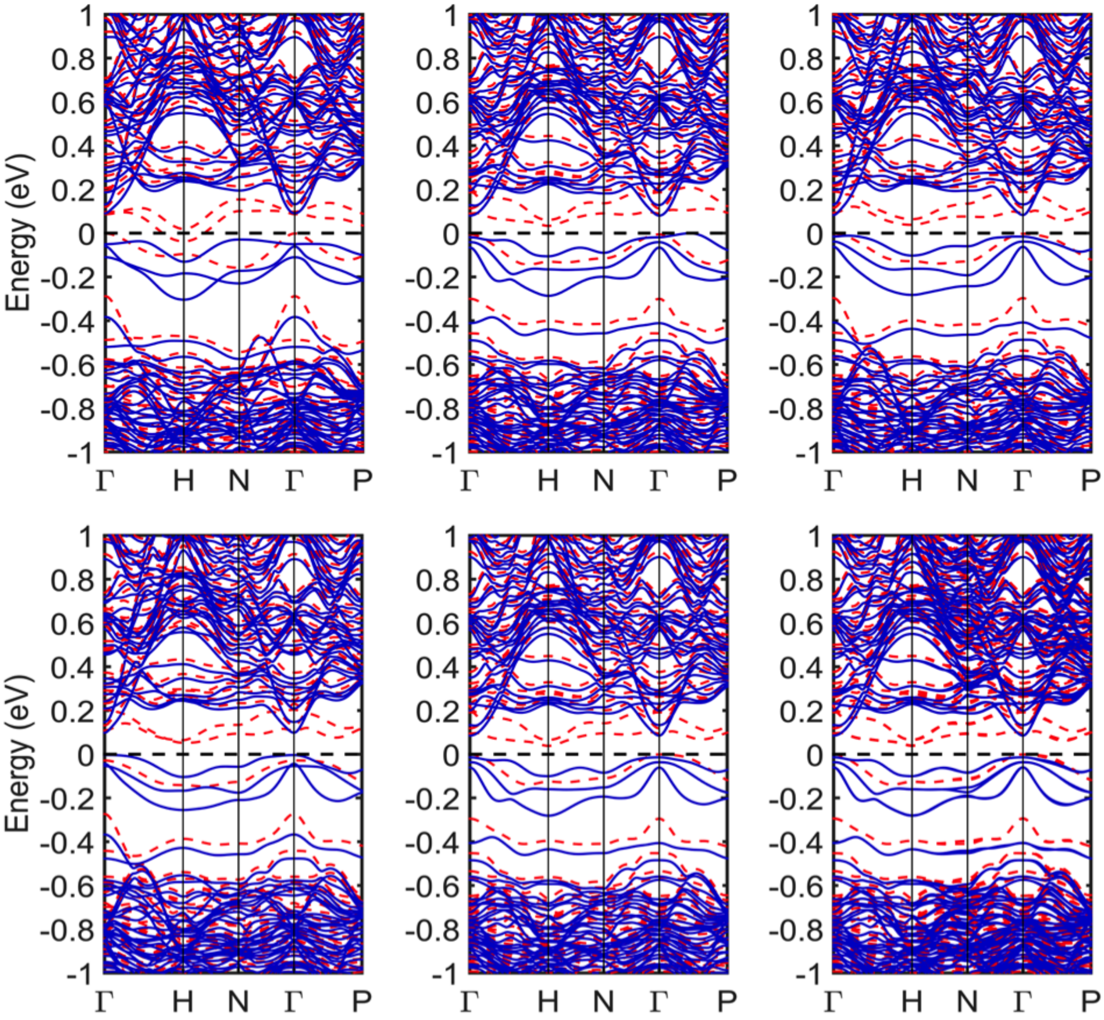

Figure 7.3: Band structures of single Sb atom vacancy in $2 \times 2 \times 2$ $La_{0.125}Co_4Sb_{11.875}$ primitive cell. The vacant Sb atom is randomly selected. The blue line represents the contribution from spin-up electrons and the red line represents the contribution from spin-down electrons.

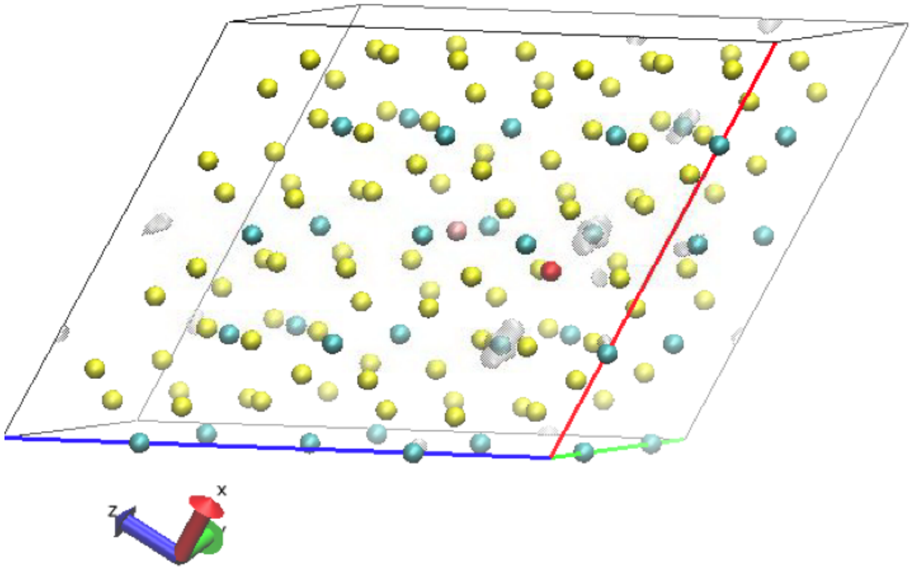

Figure 7.4: Partial charge density of single Sb vacancy band structure. Yellow atoms are Co, blue atoms are Sb, central purple atom is filled one La atom. The red circle represents a single Sb vacancy, the grey transparent surfaces are total partial charge density (including spin up+ spin down). This partial charge density mainly comes from Sb atoms nearby the vacant Sb position.

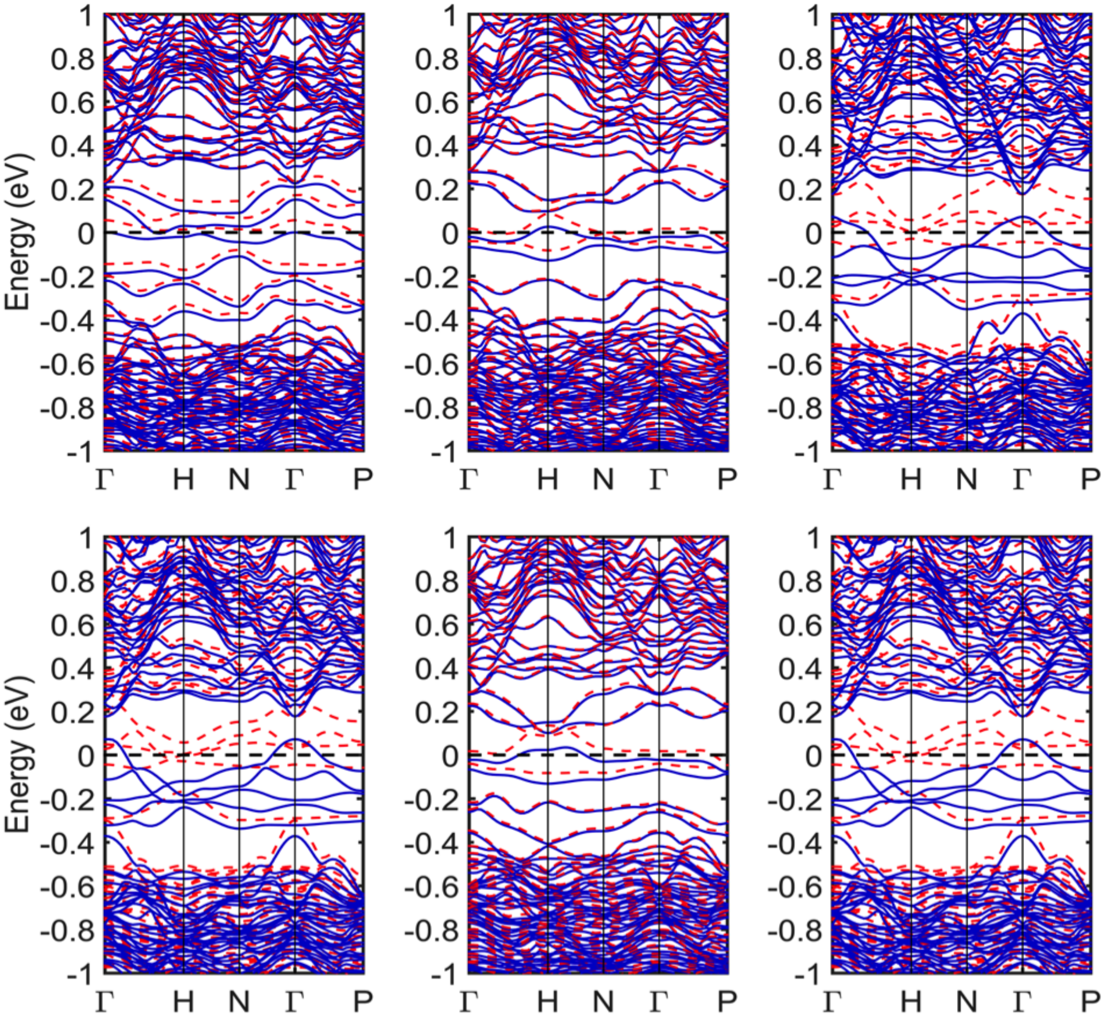

Figure 7.5: Band structure of Sb atom di-vacancy in 2 × 2 × 2 $La_{0.125}Co_4Sb_{11.75}$ primitive cell. The di-vacancy Sb atoms are connected and combinations are randomly selected. The blue line represents the contribution from spin-up electrons and the red line represents the contribution from spin-down electrons.

7.4 Conclusion and Future work

So from all the band structures shown above and comparisons that involve the variation of filling content as well as the deficiencies amount. Two questions were solved: *i)* When considering Sb deficiencies, the band structure indicates a n to p type change with La addition which perfectly matches our experimental results. *ii)* The interaction between Fermi level and the dispersive impurity bands in the band gap provides evidence of strong interaction between La filler and surrounding Sb atoms/deficiencies, this directly proved the "filler" identity of La. And again, with the ZT improved to 0.4 for $La_{0.6}Co_4Sb_{12}$, it is assured that even without being a "rattler", La, as a filler, can still contribute to improve TE property.

However, one issue still remained unsolved. That is the occurrence of the dispersive impurity bands with Sb deficiencies. Normally, impurity bands tend to be heavy with huge effective mass. Our results showed that the impurity bands from Sb deficiencies are very dispersive and close to Fermi level, which means they actually contribute to electrical property. Also, the addition of La would only shift the Fermi level, which indicates that the increasing of electrical conductivity with La addition may be due to the continuously shifting up of Fermi level that touches the impurity dispersive bands, and it is Sb deficiency that contribute to electrical conductivity instead of La, although it seems from the experiment result that the electrical conductivity is increasing with the addition of La. This answer still needs more experimental supports and can be left as future work.

Another issue remained puzzled is the strong spin polarization in $La_{0.125}Co_4Sb_{11.875}$, it is very self-explanatory from the band structure that only spin-up electrons are contributing to electrical properties. And with the increasing of the amount of Sb deficiencies (in $La_{0.125}Co_4Sb_{11.75}$), the weight of spin-up and spin-down electrons contribution were hard to be differentiated although the spin polarization still exist. This has never been observed in any Skutterudites materials nor any other TE materials before. If can be verified experimentally, a wide application field in spintronics solid state devices would be opened for filled Skutterudite materials.

Appendices

Appendix A Electron band structures and related norms

Electron band structure and density of states. Band structure describes the relation of E and k, which are the eigenvalue of energy and momentum respectively from solving schrodinger equation. Fig. 6 (a) presents the band structure of silicon, the y-axis is the energy and x-axis is the wavevector. All the captial greek letters represents the high symmetry points on brillouin zone. For more introduction about brillouin zone, you can refer to *Introduction to solid state physics* by *C Kittel* [16]. This band structure provides a blueprint of what state (E, k) are available for electrons to occupy in reciprocal space. The electrons would occupy the states with the lowest energy first, and the energy level below which all states are occupied and above which all states are empty is called the **Fermi level**. In Fig. 6 (a), the dash line represents the Fermi level.

The band structure is a good way to visualize the wavevector-dependence of energy states, and the possible electronic transitions. However,the actual transition process depends on how many states are available in both the initial and final energies. The band structure is not a reliable guide here. Hence, a full density of states across the whole Brillouin zone will become handy. Fig. 6 (b) shows the full density of states of silicon.

Fermi-Dirac statistics and Fermi "window" factor. Bands or density of states provide the available states for electrons, yet not every single state has the possibility to be occupied by electrons. The Fermi-Dirac distribution function, provides the

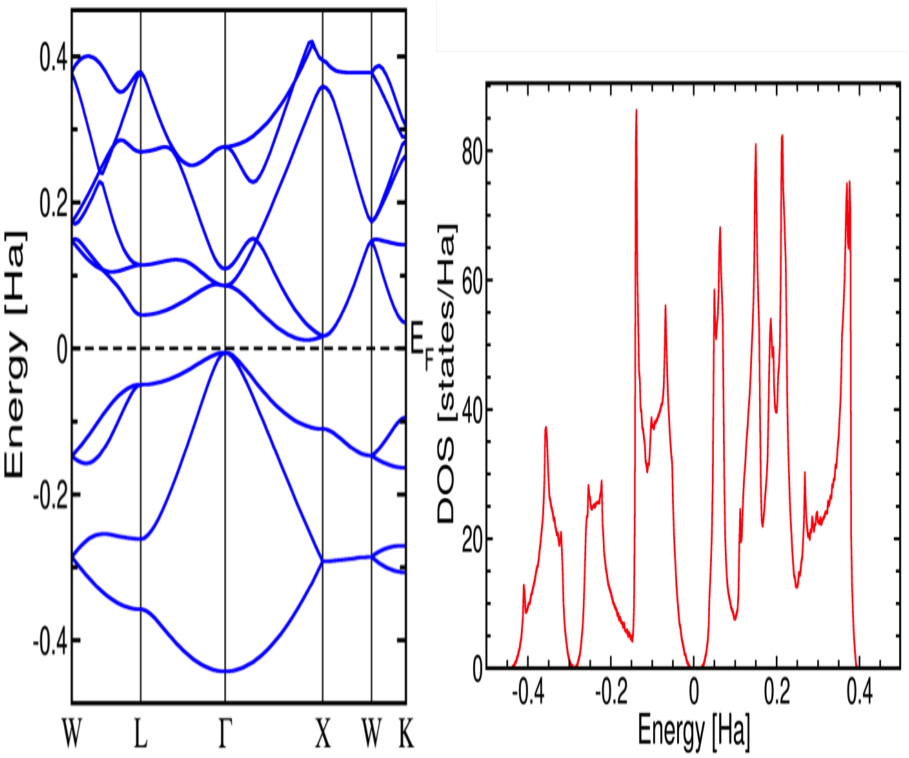

Figure 6: (a) Band structure of Si. (b) Total density of states of Si.

probability of occupancy of energy levels by electrons (Fermions).

$$f(\epsilon) = \frac{1}{e^{(E-\mu)/k_BT} + 1} \tag{1}$$

where $f(\epsilon)$ is the occupation probability of a state of energy ϵ, k_B is Boltzmann's constant, μ is the chemical potential (Fermi level when at zero temperature) and T is the temperature in Kelvin. Fig. 7 shows how the Fermi-Dirac distribution would change with temperature. From this figure it is clear that at absolute zero the distribution is a step function. It has the value of 1 for energies below the Fermi level, and a value of 0 for energies above. For finite temperatures the distribution gets smeared out, as some electrons begin to be thermally excited to energy levels above the chemical potential, μ. If taking derivative of $f(\epsilon)$ with respect to energy ϵ, the Fermi "window" factor $\frac{\partial f(\epsilon)}{\partial \epsilon}$ can be obtained. It is a bell-shape function centered at $E = E_f$, having a width of $\approx k_BT$. The Fermi window can be interpreted as a direct consequence of Pauli exclusion principle, it shows that at a finite temperature only electrons near the Fermi surface contribute to the conduction process. We will use this in the definition of α and σ later. Usually the number of electrons can be obtained by multiplying density of states with Fermi-Dirac distribution.

Effective mass. Effective mass is another parameter that can describe the electrons' behavior obtained from band structure. It is a quantity that is used to simplify band structures by constructing an analogy to the behavior of a free particle with that mass [16]. It is defined as

$$(\frac{1}{m^*})_{\mu\nu} = \frac{1}{\hbar^2}\frac{d^2E(k)}{dk_\mu dk_\nu} \tag{2}$$

In a three dimensional band structure, the effective mass is a tensor. It also reflects

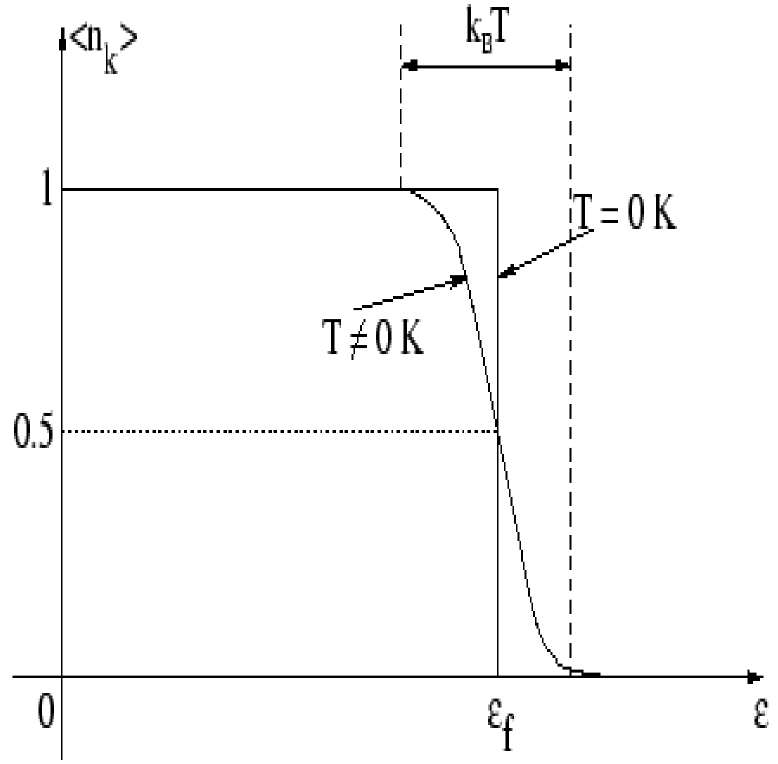

Figure 7: The Fermi-Dirac distribution at T=0K and finite temperature. The $k_B T$ range means only the electrons close to Fermi level are constructive to electrical transport properties.

the inverse of the band curvature: the lower m^*, the larger is the curvature. Sometimes, when the effective mass has a different value according to the direction of the wave vector k, then a *density of states effective mass* will be used for simplifying purpose. For defining α and σ in next section, the band effective mass will be used.

Semiconductor and metal. The presence of the Fermi level differentiate a semiconductor from a metal. For discussion, three terms must be defined. The highest energy band that contains electrons is called **valence band**, whereas the lowest energy empty band is called the **conduction band**. The **band gap** is the difference in energy between the valence and conduction bands. The laws of quantum mechanics forbid electrons from being in the band gap, thus, an electron must always be in one of the bands. While both semiconductor and a metal have bands and band gap, for a pure (intrinsic) semiconductor, the Fermi level usually lies in the band gap; for a metal, the Fermi level is far deep into either the conduction band or valence band (at least above $\approx 5k_BT$ from the band edges).

Intrinsic and Extrinsic Semiconductors. Knowing that semiconductor has a band structure with band gap between conduction and valence band, and the Fermi level lies in the gap, so electrons from valence band should excite across the band gap into the conduction band in order to contribute to the electrical property. At finite temperatures the only charge carriers are the electrons from the conduction band and holes(can be seen as a carrier with positive charge) from the valence band that arises as a result of the thermal excitation of electrons to the conduction band. These charge carriers are called *intrinsic* charge carriers, and necessarily there are equal numbers of electrons and holes. In this case, the semiconductor can be called **intrinsic semiconductor**. However, in most of the cases, the electrical conductivity is still orders of magnitude lower than that of a metal. Therefore, by introducing a different kind of atom into the intrinsic semiconductor, the electronic structure can be modified so as to improve the electrical conductivity. Two different kinds of atoms should be discussed here: When the electrons of the additional atoms are bound only weakly to their parent impurity atoms, and even at very low temperatures these electrons can be promoted into the conduction band of the semiconductor. This is often represented schematically in band diagrams by the addition of 'donor levels' just below the bottom of the conduction band, as in Fig. 8 (a). The dotted line represents the existence of additional electrons which may be easily excited into the conduction band. Semiconductors that have been doped in this way will have a surplus of electrons, and are called **n-type semiconductors**. In such semiconductors, electrons are the majority carriers. Conversely, if the addtional atoms cause a deficit in the number of valence electrons in the material. This introduces electron-accepting levels just above the top of the valence band, and causes more holes to be introduced into the valence band, as in Fig. 8. Hence, the majority charge carriers are positive holes in this case. Semiconductors doped in this way are termed **p-type semiconductors.** Doped semiconductors (either n-type or p-type) are known as **extrinsic semiconductors.** This thesis mainly focus on doped semiconductors.

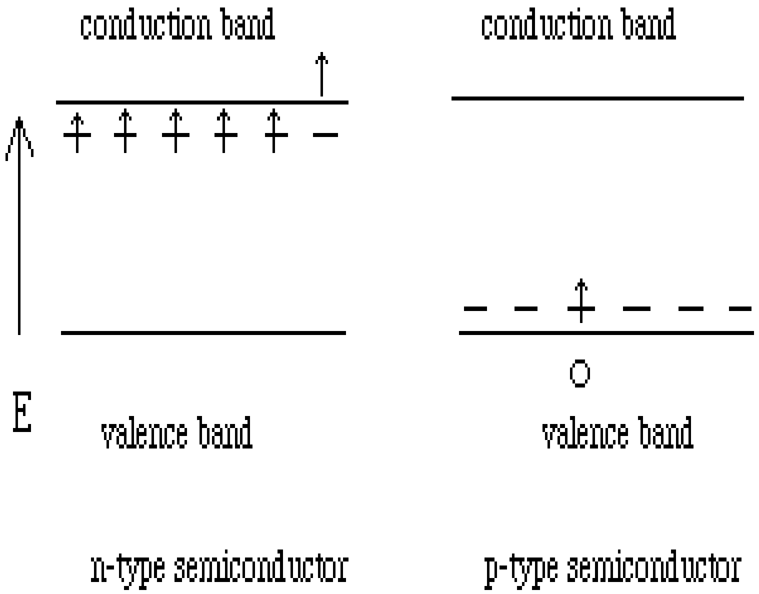

Figure 8: A schematic figure of n-type semiconductor and p-type semiconductor.

Appendix B Electron transport: mobility

By definition, the mobility of electrons characterizes how quickly an electron react to an applied field. The most basic mobility is called drift mobility, which is derived from $v = \frac{e\tau}{m}E$. τ is the relaxation time, characterizing the time traveling between two collisions for an electron, E is the applied field and v is the corresponding velocity. The term $\frac{e\tau}{m}$ is called mobility μ. As we can see here, μ is closely related to τ.

In real materials, electrons not only can be scattered by electrons, they can also be scattered by phonons, boundaries *etc.* Therefore, the energy dependent mobility $\mu(E)$ in equation 1.16 will get its value depend on what scattering mechanism electrons experience. For easy reference, the characteristic mobility and relaxation time of a few non-resonant scattering schemes in thermoelectricity are listed below:

For electron scattering by acoustic phonon modes, the relaxation time calculated based on a deformation-potential model is

$$\tau_e = \frac{h^4 v^2 \rho_d E^{-1/2}}{(8\pi^2)^{3/2} k_B T \Delta^2 (m^*)^{3/2}} \tag{3}$$

where ρ_d is the density, m^* the effective mass, and Δ the deformation-potential constant. The corresponding mobility is

$$\mu = \frac{(8\pi)^{1/2} e h v^2 \rho_d}{3 k_B^{3/2} \Delta^2} (m^*)^{-5/2} T^{-3/2} \tag{4}$$

State of the art TE materials often possess a unit cell with many atoms, hence optical modes are another major source of electron scattering, especially at elevated temperatures. One should note that the relaxation time approximation doesn't hold for polar optical code scattering. Nonetheless, the validity of the relaxation time approximation is justified at elevated temperatures, in which case the relaxation time and mobility are:

$$\tau_e \propto \frac{E^{1/2}}{(m^*)^{1/2}}T \quad and \quad \mu \propto (m^*)^{-3/2}T^{-1/2} \tag{5}$$

For electron scattering by ionized-impurity scattering, the correspondent relaxation time and mobility are,

$$\tau_e = \frac{8(2)^{1/2}(m^*)^{1/2}\varepsilon^2 E^{3/2}}{\pi^{3/2}N_i e^4 N}[1+(\frac{3\varepsilon k_B T}{e^2 N_i^{1/3}})^2]^{-1} \quad and \quad \mu \propto T^{3/2} \tag{6}$$

where N_i is the impurity concentration. For electron scattering by charge neutral grain boundary, the correspondent mobility is

$$\mu = \frac{el}{\sqrt{8k_B \pi T m^*}}e^{-\frac{E_B}{k_B T}} \tag{7}$$

where E_B is the mean energetic barrier between grains, and l the mean grain size.

Appendix C Thermal conductivity

Thermal conductivity κ is defined as the energy transmitted per unit time across unit area per unit temperature gradient.

$$j = -\kappa \frac{dT}{dx} \tag{8}$$

Dependence of κ on dT/dx implies that the thermal energy transfer is a random process involving scattering, which introduces mean free path of phonons in the problem. We make a relaxation time kind of approximation: the energy contributed by a phonon at a point is decided by where it has had its last collision. So phonons coming from the high temperature end bring more energy than those coming from the low temperature end. Thus although there is no net number flux, there can be energy flux travelling from the high T end to the low T end.

Temperature at two ends of a one dimensional rod are $(T + \Delta T)$ and T. The temperature at point x is $T(x)$ and the energy at that point is $E(T(x))$. Half the phonons arriving at a point x are from the high temperature side each carrying an energy $E(T(x - \upsilon_x \tau))$, the other half are from the low T side and carry an energy $E(T(x + \upsilon_x \tau))$. Number of phonons arriving at x per unit time per unit area of cross section is $1/2n\upsilon_x$, where υ_x is the phonon speed in x direction. So the net energy flux is :

$$j = \frac{1}{2} n\upsilon (T(x - \upsilon_x \tau)) - E(T(x + \upsilon_x \tau))] = n\upsilon_x^2 \tau \frac{dE}{dT}(-\frac{dT}{dx}) = -\frac{1}{3}\upsilon^2 \tau C_v \frac{dT}{dx} \tag{9}$$

Therefore,

$$\kappa = \frac{1}{3} C_v \upsilon^2 \tau = \frac{1}{3} C_v l \upsilon \tag{10}$$

So lattice thermal conductivity of a crystal is determined by two contributions-specific heat and mean free path of phonons.

Appendix D A brief review of the development of thermoelectric generators

Throughout the history of science, the discoveries of great phenomena or principles is always followed by people's motivation to put them in practice. Before we delve into more physical details about thermoelectric performance, it is necessary to take a look on some of the developments of thermoelectric devices based on thermoelectric effect in history [71–75].Since Seebeck effect was discovered, various attempts were made to use the electromotive force (emf)of the thermogenerators. In 19^{th} century, there is this device called "thermopile" developed by Leopoldo Nobili and Macedonio Melloni, it has a number of thermocouples connected in series and is used for the measurement of temperature and infrared radiation, which also served as a stable power supply for physical experiments by Georg Simon Ohm. And then came the "Markus"thermopile (1864)(Fig. 9),The emf of a single thermocouple was called "one twentieth of a Daniel cell" and generated about 55 mV. The negative leg consisted of a 10:6:6 copper-zinc-nickel alloy, the positive leg of a 12:5:1 antimony-zinc-bismuth alloy. But it has a disadvantage of the strong oxidation of the contacts that would increase the internal resistance. And then came the Becquerel thermopile, Clamond thermopile, The Noe thermopile and Hauck thermopile *et al* [71].

When the 20^{th} centry came, new design on devices were developed, in 1925, Thermattaix was made for loading lead-acid accumulators (Fig. 10). Around 1950, power in the kW range was generated in the Russian nuclear reactor "Romoschka" with thermogenerators. In 1958, A. F. Joffe described the application of the thermoelectric effect for the use of the bulb heat. From the seventies to the nineties "Radioscope Thermoelectric Generators"(RTGs) are used in the space missions "Pioneer

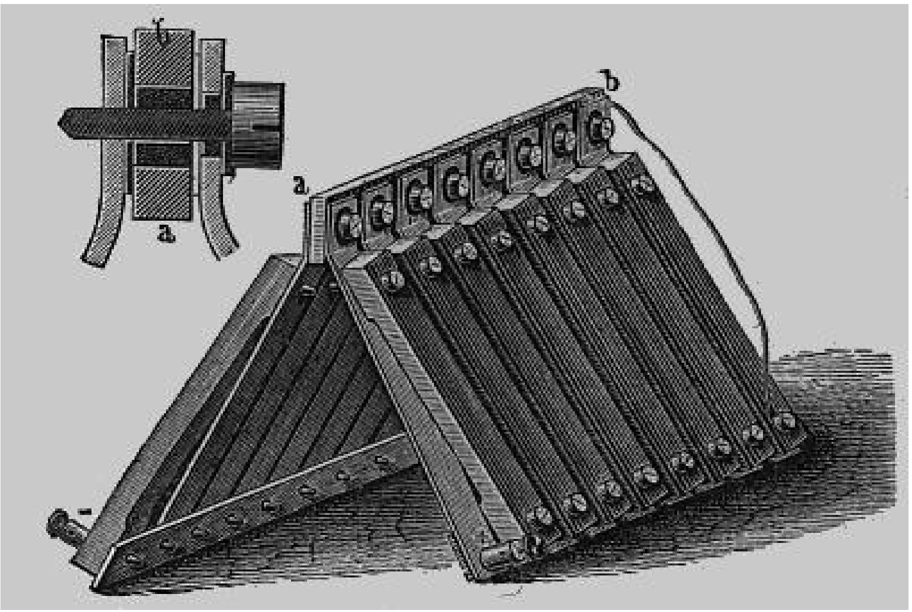

Figure 9: Markus thermopile [71].

Figure 10: Thermattaix

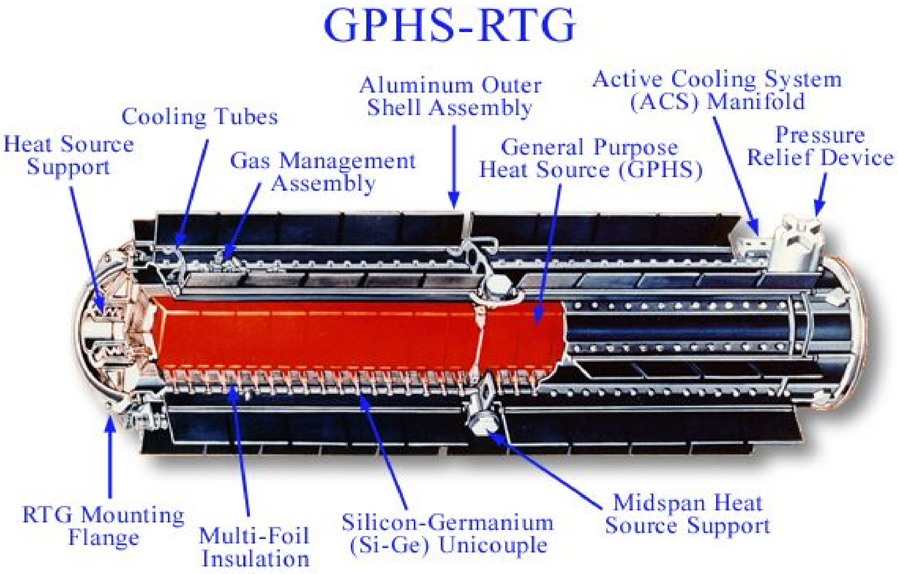

Figure 11: Cross-sectional view of an RTG

10”,”Pioneer 11”, ”Voyager I”,”Voyager II”,”Galileo”,”Ulysses”,”Cassini” and ”New Horizons” as power supplies of the space capsules(Fig. 11). In the Voyager mission an RTG consisted of 300 thermocouples. Since 1977 these thermogenerators still operate free from maintenance.

Bibliography

[1] GS Nolas, DT Morelli, and Terry M Tritt. Skutterudites: A phonon-glass-electron crystal approach to advanced thermoelectric energy conversion applications. *Annual Review of Materials Science*, 29(1):89–116, 1999.

[2] DM Rowe and CM Bhandari. *Modern Thermoelectricity.* London: Holt Saunders, 2002.

[3] Xinfeng Tang Han Li. *High Performance Nanostructured Filled Skutterudite Thermoelectric Materials Prepared by Melt-spinning.* Wuhan University of Technology Press, 2012.

[4] Tim Sands. Designing nanocomposite thermoelectric materials, Feb 2016. nanohub.org/resources/395/download/2005.11.08-sands.pdf.

[5] G Jeffrey Snyder and Eric S Toberer. Complex thermoelectric materials. *Nature materials*, 7(2):105–114, 2008.

[6] Jennifer Whitney Graff. *EXCEEDING THE FILLING FRACTION LIMIT:AN APPROACH TO ENHANCEMENT OF THERMOELECTRIC PROPERTIES OF FILLED-*Co_4Sb_{12}. PhD thesis.

[7] Terry M Tritt. Thermoelectric phenomena, materials, and applications. *Annual review of materials research*, 41:433–448, 2011.

[8] V Yu Irkhin and Yu P Irkhin. *Electronic structure, correlation effects and physical properties of d-and f-metals and their compounds.* Cambridge Int Science Publishing, 2007.

[9] Ali Shakouri, Chris LaBounty, Patrick Abraham, Joachim Piprek, and John E Bowers. Enhanced thermionic emission cooling in high barrier superlattice heterostructures. In *MRS Proceedings*, volume 545, page 449. Cambridge Univ Press, 1998.

[10] Daryoosh Vashaee and Ali Shakouri. Conservation of lateral momentum in heterostructure integrated thermionic coolers. In *MRS Proceedings*, volume 691, pages G6–5. Cambridge Univ Press, 2001.

[11] Ali Shakouri. Nanoscale devices for solid state refrigeration and power generation. In *Semiconductor Thermal Measurement and Management Symposium, 2004. Twentieth Annual IEEE*, pages 1–9. IEEE, 2004.

[12] JO Sofo and GD Mahan. Optimum band gap of a thermoelectric material. *Physical Review B*, 49(7):4565, 1994.

[13] LD Hicks and MS Dresselhaus. Effect of quantum-well structures on the thermoelectric figure of merit. *Physical Review B*, 47(19):12727, 1993.

[14] Kenji Koga, Koji Akai, Kazunori Oshiro, and Mitsuru Matsuura. Electronic structure and optical properties of binary skutterudite antimonides. *Physical Review B*, 71(15):155119, 2005.

[15] R Franz and G Wiedemann. Ueber die wärme-leitungsfähigkeit der metalle. *Annalen der Physik*, 165(8):497–531, 1853.

[16] Charles Kittel. *Introduction to solid state physics*. Wiley, 2005.

[17] Yufei Liu, Menghan Zhou, and Jian He. Towards higher thermoelectric performance of bi 2 te 3 via defect engineering. *Scripta Materialia*, 111:39–43, 2016.

[18] Joseph P Heremans, Bartlomiej Wiendlocha, and Audrey M Chamoire. Resonant levels in bulk thermoelectric semiconductors. *Energy & Environmental Science*, 5(2):5510–5530, 2012.

[19] Y Zhang, XL Wang, WK Yeoh, RK Zheng, and C Zhang. Electrical and thermoelectric properties of single-wall carbon nanotube doped bi2te3. *Applied Physics Letters*, 101(3):031909, 2012.

[20] BC Sales, D Mandrus, and R KIFILLED Williams. Filled skutterudite antimonides: a new class of thermoelectric materials. *Science*, 272(5266):1325–1328, 1996.

[21] H Scherrer and S Scherrer. Thermoelectric handbook–macro to nano. *ed. Rowe, DM, Taylor & Francis*, 2006.

[22] JO Sofo and GD Mahan. Electronic structure of cosb 3: A narrow-band-gap semiconductor. *Physical Review B*, 58(23):15620, 1998.

[23] Yinglu Tang, Yuting Qiu, Lili Xi, Xun Shi, Wenqing Zhang, Lidong Chen, Ssu-Ming Tseng, Sinn-wen Chen, and G Jeffrey Snyder. Phase diagram of in–co–sb system and thermoelectric properties of in-containing skutterudites. *Energy & Environmental Science*, 7(2):812–819, 2014.

[24] I Lefebvre-Devos, M Lassalle, X Wallart, J Olivier-Fourcade, L Monconduit, and JC Jumas. Bonding in skutterudites: Combined experimental and theoretical characterization of cosb 3. *Physical Review B*, 63(12):125110, 2001.

[25] Banaras Khan, HA Rahnamaye Aliabad, S Jalali-Asadabadi, Imad Khan, Iftikhar Ahmad, et al. Electronic band structures of binary skutterudites. *Journal of Alloys and Compounds*, 647:364–369, 2015.

[26] Lukas Hammerschmidt, Sabine Schlecht, and Beate Paulus. Electronic structure and the ground-state properties of cobalt antimonide skutterudites: Revisited with different theoretical methods. *physica status solidi (a)*, 210(1):131–139, 2013.

[27] David J Singh and Warren E Pickett. Skutterudite antimonides: Quasilinear bands and unusual transport. *Physical Review B*, 50(15):11235, 1994.

[28] LD Dudkin and N Kh Abrikosov. On the doping of the semiconductor compound cosb3. *Soviet Physics-Solid State*, 1(1):126–133, 1959.

[29] T Caillat, A Borshchevsky, and J-P Fleurial. Properties of single crystalline semiconducting cosb3. *Journal of Applied Physics*, 80(8):4442–4449, 1996.

[30] GS Nolas, GA Slack, T Caillat, and GP Meisner. Raman scattering study of antimony-based skutterudites. *Journal of applied physics*, 79(5):2622–2626, 1996.

[31] D Mandrus, A Migliori, TW Darling, MF Hundley, EJ Peterson, and JD Thompson. Electronic transport in lightly doped cosb 3. *Physical Review B*, 52(7):4926, 1995.

[32] E Arushanov, M Respaud, H Rakoto, JM Broto, and T Caillat. Shubnikov–de haas oscillations in cosb 3 single crystals. *Physical Review B*, 61(7):4672, 2000.

[33] Wenyu Zhao, Ping Wei, Qingjie Zhang, Hua Peng, Wanting Zhu, Dingguo Tang, Jian Yu, Hongyu Zhou, Zhiyuan Liu, Xin Mu, et al. Multi-localization transport behaviour in bulk thermoelectric materials. *Nature communications*, 6, 2015.

[34] Daehyun Wee, Boris Kozinsky, Nicola Marzari, and Marco Fornari. Effects of filling in cosb 3: Local structure, band gap, and phonons from first principles. *Physical Review B*, 81(4):045204, 2010.

[35] Swetarekha Ram, V Kanchana, and MC Valsakumar. Skutterudites under pressure: An ab initio study. *Journal of Applied Physics*, 115(9):093903, 2014.

[36] George S Nolas, H Takizawa, T Endo, H Sellinschegg, and DC Johnson. Thermoelectric properties of sn-filled skutterudites. *Applied Physics Letters*, 77(1):52–54, 2000.

[37] Xinfeng Tang, Lidong Chen, Takashi Goto, and Toshio Hirai. Effects of ce filling fraction and fe content on the thermoelectric properties of co-rich ce y fe x co 4-x sb 12. *Journal of Materials Research*, 16(03):837–843, 2001.

[38] Brian C Sales. Novel thermoelectric materials. *Current Opinion in Solid State and Materials Science*, 2(3):284–289, 1997.

[39] Donald T Morelli, Gregory P Meisner, Baoxing Chen, Siqing Hu, and Ctirad Uher. Cerium filling and doping of cobalt triantimonide. *Physical Review B*, 56(12):7376, 1997.

[40] GS Nolas, JL Cohn, and GA Slack. Effect of partial void filling on the lattice thermal conductivity of skutterudites. *Physical Review B*, 58(1):164, 1998.

[41] Xinfeng Tang, Qingjie Zhang, Lidong Chen, Takashi Goto, and Toshio Hirai. Synthesis and thermoelectric properties of p-type-and n-type-filled skutterudite rymxco4-xsb12 (r: Ce, ba, y; m: Fe, ni). *Journal of Applied Physics*, 97(9):3712, 2005.

[42] Hiroyuki Kitagawa, Masayuki Hasaka, Takao Morimura, Hiromichi Nakashima, and Shin-ichiro Kondo. Skutterudite structure and thermoelectric property in ce f fe 8- x co x sb 24 (f= 0–2, x= 0–8). *Materials research bulletin*, 35(2):185–192, 2000.

[43] JL Feldman, David J Singh, C Kendziora, David Mandrus, and Brian C Sales. Lattice dynamics of filled skutterudites: La (f e, c o) 4 sb 12. *Physical Review B*, 68(9):094301, 2003.

[44] LD Chen, T Kawahara, XF Tang, T Goto, T Hirai, Jeffrey S Dyck, W Chen, and C Uher. Anomalous barium filling fraction and n-type thermoelectric performance of bayco4sb12bayco4sb12. 2001.

[45] X Shi, W Zhang, LD Chen, and J Yang. Filling fraction limit for intrinsic voids in crystals: Doping in skutterudites. *Physical review letters*, 95(18):185503, 2005.

[46] X Shi, W Zhang, LD Chen, J Yang, and C Uher. Thermodynamic analysis of the filling fraction limits for impurities in cosb 3 based on ab initio calculations. *Acta Materialia*, 56(8):1733–1740, 2008.

[47] X Shi, H Kong, C-P Li, C Uher, J Yang, JR Salvador, H Wang, L Chen, and W Zhang. Low thermal conductivity and high thermoelectric figure of merit in n-type baxybyco4sb12 double-filled skutterudites. *Applied Physics Letters*, 92(18):182101, 2008.

[48] WY Zhao, CL Dong, P Wei, W Guan, LS Liu, PC Zhai, XF Tang, and QJ Zhang. Synthesis and high temperature transport properties of barium and indium double-filled skutterudites baxinyco4sb12-z. *Journal of Applied Physics*, 102(11):3708, 2007.

[49] H Anno, T Sakakibara, Y Notohara, H Tashiro, T Koyanagi, H Kaneko, and K Matsubara. Preparation and thermoelectric properties of cosb 3 thin films on gaas (100) substrate. In *Thermoelectrics, 1997. Proceedings ICT'97. XVI International Conference on*, pages 338–342. IEEE, 1997.

[50] Muhammet S Toprak, Christian Stiewe, Dieter Platzek, Simon Williams, Luca Bertini, Eckhard Muller, Carlo Gatti, Yu Zhang, Michael Rowe, and Mamoun Muhammed. The impact of nanostructuring on the thermal conductivity of thermoelectric cosb3. *Advanced Functional Materials*, 14(12):1189–1196, 2004.

[51] V Savchuk, A Boulouz, S Chakraborty, J Schumann, and H Vinzelberg. Transport and structural properties of binary skutterudite cosb3 thin films grown by dc magnetron sputtering technique. *Journal of applied physics*, 92(9):5319–5326, 2002.

[52] PN Alboni, X Ji, Jian He, N Gothard, and Terry M Tritt. Thermoelectric properties of la0. 9cofe3sb12–cosb3 skutterudite nanocomposites. *Journal of Applied Physics*, 103(11):113707, 2008.

[53] Jing-Feng Li, Wei-Shu Liu, Li-Dong Zhao, and Min Zhou. High-performance nanostructured thermoelectric materials. *NPG Asia Materials*, 2(4):152–158, 2010.

[54] Binary phase diagram of co-sb, January 2016. www.crct.polymtl.ca/fact/phase_diagram.php?file=Co-Sb.jpg&dir=SGTE2011.

[55] Dale Hitchcock, Roger Livingston, and Donald Liebenberg. Improved understanding of the spark plasma sintering process. *Journal of Applied Physics*, 117(17):174505, 2015.

[56] M Tokita. Mechanism of spark plasma sintering. In *Proceeding of NEDO International Symposium on Functionally Graded Materials*, volume 21, page 22. Japan, 1999.

[57] Laser flash, January 2016. www.netzsch-thermal-analysis.com/us/products-solutions/thermal-diffusivity-conductivity/lfa-457-microflash/.

[58] Robert D Cowan. Pulse method of measuring thermal diffusivity at high temperatures. *Journal of Applied Physics*, 34(4):926–927, 1963.

[59] JoAo Cape and GW Lehman. Temperature and finite pulse-time effects in the flash method for measuring thermal diffusivity. *Journal of applied physics*, 34(7):1909–1913, 1963.

[60] Jürgen Blumm and Johannes Opfermann. Improvement of the mathematical modeling of flash measurements. *High Temperatures. High Pressures*, 34(5):515–521, 2002.

[61] AL Pope, B Zawilski, and TM Tritt. Description of removable sample mount apparatus for rapid thermal conductivity measurements. *Cryogenics*, 41(10):725–731, 2001.

[62] Georg Kresse and Jürgen Hafner. Ab initio molecular dynamics for liquid metals. *Physical Review B*, 47(1):558, 1993.

[63] Georg Kresse and Jürgen Furthmüller. Efficient iterative schemes for ab initio total-energy calculations using a plane-wave basis set. *Physical Review B*, 54(16):11169, 1996.

[64] Peter E Blöchl. Projector augmented-wave method. *Physical Review B*, 50(24):17953, 1994.

[65] Georg Kresse and D Joubert. From ultrasoft pseudopotentials to the projector augmented-wave method. *Physical Review B*, 59(3):1758, 1999.

[66] John P Perdew, Kieron Burke, and Matthias Ernzerhof. Generalized gradient approximation made simple. *Physical review letters*, 77(18):3865, 1996.

[67] JH Van Vleck. Quantum mechanics-the key to understanding magnetism. *Reviews of Modern Physics*, 50(2):181, 1978.

[68] Hiroshi Mizoguchi and Hideo Hosono. La 2 sb, a layered superconductor with metal–metal bonds. *Chemical Communications*, 47(13):3778–3780, 2011.

[69] Terry M Tritt. *Thermal conductivity: theory, properties, and applications.* Springer Science & Business Media, 2005.

[70] Lukas Hammerschmidt, Marcel Quennet, Kai Töpfer, and Beate Paulus. Low-index surfaces of cosb 3 skutterudites from first principles. *Surface Science*, 637:124–131, 2015.

[71] Thermo-electric generators, January 2016. www.dself.dsl.pipex.com/MUSEUM/POWER/thermoelectric/thermoelectric.htm.

[72] Die theorie, January 2016. www.seebeck-elemente.de/de/download/theorie.pdf.

[73] Thermogeneratoren, January 2016. www.seebeck-elemente.de/de/download/wie_sinnvoll_ist_der_einsatz_von_thermogeneratoren.pdf.

[74] FD Rosi, B Abeles, and RV Jensen. Materials for thermoelectric refrigeration. *Journal of Physics and Chemistry of Solids*, 10(2):191–200, 1959.

[75] Radioisotope thermoelectric generator, January 2016. en.wikipedia.org/wiki/Radioisotope_thermoelectric_generator#Use.